

RSC Advances



This is an *Accepted Manuscript*, which has been through the Royal Society of Chemistry peer review process and has been accepted for publication.

Accepted Manuscripts are published online shortly after acceptance, before technical editing, formatting and proof reading. Using this free service, authors can make their results available to the community, in citable form, before we publish the edited article. This *Accepted Manuscript* will be replaced by the edited, formatted and paginated article as soon as this is available.

You can find more information about *Accepted Manuscripts* in the [Information for Authors](#).

Please note that technical editing may introduce minor changes to the text and/or graphics, which may alter content. The journal's standard [Terms & Conditions](#) and the [Ethical guidelines](#) still apply. In no event shall the Royal Society of Chemistry be held responsible for any errors or omissions in this *Accepted Manuscript* or any consequences arising from the use of any information it contains.

Impact of Gd³⁺-substitution on the structural, magnetic and electrical properties of cobalt ferrite nanoparticles

C. Murugesan* and G. Chandrasekaran

Department of Physics, School of Physical, Chemical and Applied Sciences,
Pondicherry University, Puducherry - 605014, India.

*E-mail address: murugesanscience@gmail.com. Mobile: +919600564874

Abstract

In this work, we have focused on the influence of Gd³⁺ substitution in structural, magnetic and electrical properties of cobalt ferrite synthesized by using sol-gel auto combustion method. The powder x-ray diffraction analysis reveals that the Gd-substituted cobalt ferrites crystallize in single phase spinel structure for lower concentrations of Gd³⁺, while a trace of GdFeO₃ appears as a minor phase for higher concentrations. Raman and Fourier transform infrared spectra confirm the formation of spinel structure. Furthermore, Raman analysis shows that the inversion degree of cobalt ferrite decreases with Gd³⁺ doping. The field emission scanning electron microscopy images show that the substitution of small amount of Gd³⁺ causes considerable reduction of grain size. Studies on magnetic properties reveal that the coercivity of Gd-substituted cobalt ferrites enhances from 1265 Oe to 1635 Oe and the saturation magnetization decreases monotonically from 80 emu/g to 53.8 emu/g and the magnetocrystalline anisotropy constant increases from 5.8×10^5 erg/cm³ to 2.23×10^6 erg/cm³ at 300 K. The electrical properties show that the Gd³⁺ doped samples exhibit the high values of dielectric constant (616 at 100 Hz) and ac conductivity (4.83×10^{-5} S/cm at 100 Hz) at room temperature. The activation energy is found to decrease from 0.408 to 0.347 eV in for the rise of Gd³⁺ content. The impedance study

brings out role of bulk grain and grain-boundary towards the electrical resistance and capacitance of cobalt ferrite. Gd-substitution and nano size of cobalt ferrite enhance the electrical and magnetic properties which could ensure a higher memory storage capability.

Introduction

Spinel ferrites with the general formula MFe_2O_4 (M-Co, Ni, Mn and Zn etc.) are the most interesting magnetic oxides due to their superior electrical, magnetic and optical properties¹⁻⁸. Among the spinel ferrites, cobalt ferrite is an attractive candidate due to its significant properties such as high coercivity, high electrical resistivity, moderate saturation magnetization, large magnetocrystalline anisotropy ($\sim 4 \times 10^6$ ergs/cm³), good chemical stability and high Curie temperature (793 K)⁹⁻¹⁶. It is of significant technological interests due to its potential applications in targeted drug delivery systems^{17, 18}, microwave devices^{19, 20}, sensors²¹, catalysis^{22, 23} and magnetic recording applications^{9, 24} etc. Recently, the doping of small amount of trivalent rare earth cations in spinel ferrite has emerged as a promising strategy to improve the magnetic and electrical properties. Moreover, these properties are governed by the antiferromagnetic super exchange interaction between Fe^{3+} - Fe^{3+} ions; introducing small amount of trivalent rare earth (RE) ions into the spinel ferrite lattices will also induce RE^{3+} - Fe^{3+} interactions²⁵⁻³⁰. It is well known that the intrinsic properties of the spinel ferrite nanoparticles depend on the chemical composition and preparative methods^{31, 32}. Spinel ferrites are prepared using several methods such as co-precipitation, flash combustion, citrate precursor, sol-gel, auto-combustion and ceramic techniques. Among them, the auto-combustion method is advantageous to synthesis nano particles due to inexpensive precursors, low external energy consumption, simple equipment requirement and uniformity of particle size³³. In the present work we aim to study the effect of Gd^{3+} substitution on the structural, magnetic and electrical properties of cobalt ferrite

nanoparticles prepared using sol-gel auto combustion method. The results suggest that the substitution of gadolinium in cobalt ferrite has substantial impact on the properties of prepared samples towards the furtherance of capacity of memory storage.

Experimental

Preparation

The nanoparticles of $\text{CoGd}_x\text{Fe}_{2-x}\text{O}_4$ ($x = 0.0, 0.05, 0.10, 0.15$ and 0.20) are synthesized using self propagating sol-gel auto-combustion method. Analytical grade cobalt nitrate, ferric nitrate, gadolinium nitrate and citric acid are used as reactants. Required amount of reactants are weighed and the molar ratio of metal nitrate to citric acid is 1:1. The weighed metal nitrates and citric acid are separately dissolved in minimum amount of double-distilled water. The obtained clear solutions are mixed together. The pH of the solution is adjusted to 7 with the addition of 25 % ammonia solution and then magnetically stirred at ambient temperature. Its homogeneous solution is allowed to condense with continuous stirring on a hot plate, at a temperature of about 85°C till it forms a highly viscous and dried gel. Then the dried viscous gel is heated on a hot plate at 300°C until it gets self ignited. The self ignited final product is ground well and then used for further characterization.

Characterization

The thermal analysis of the as prepared samples are carried out using a simultaneous thermo gravimetric and differential thermal analysis (TG-DTA) system - Q600 SDT at a step rate of $10^\circ\text{C min}^{-1}$ in an air atmosphere from 30°C to 1000°C . The powder x- ray diffraction (PXRD) pattern of all the samples are obtained using a x-ray powder diffractometer (RIGAKU, Ultima IV) employing $\text{Cu-K}\alpha$ (Wavelength- 1.5406 \AA). Raman spectra are measured using a LASER

Raman spectrophotometer (Renishaw inVia reflex) equipped with a CCD camera using Ar ion laser (514 nm) over the range of 100-900 cm^{-1} . Fourier transform infrared (FTIR) spectra are recorded using a Shimadzu-8700 FTIR spectrometer over the range of 1200–360 cm^{-1} . The surface morphology and the elemental composition of the samples are examined using a field emission scanning electron microscope (FE-SEM, Carl Zeiss SUPRA 55) equipped with energy dispersive spectroscopy (EDS). The magnetic measurements are performed using a (Quantum Design) physical property measurement system (PPMS) with a maximum applied field range of 6 T. The frequency dependence of ac electrical properties of the samples in the form of pellets (~ 10 mm in diameter and ~ 1.5 mm thickness) are measured using a LCR meter (PSM 1735 COM) in the frequency range of 100 Hz–1 MHz.

Results and discussion

Thermal analysis

The TG-DTA curves of as prepared $\text{CoGd}_x\text{Fe}_{2-x}\text{O}_4$ ($x = 0.0, 0.05, 0.1, 0.15$ and 0.2) powders are shown in Fig. 1. It is seen from Fig. 1 that there are three regions of thermal process viz; 30 - 175 $^\circ\text{C}$, 175 - 625 $^\circ\text{C}$ and 625 - 1000 $^\circ\text{C}$. In the first region (30 - 175 $^\circ\text{C}$) the initial weight loss in TGA curves and small endothermic peaks in DTA curves are due to the evaporation of moisture present in the as prepared samples. A major weight loss noticed in the second region (175 - 625 $^\circ\text{C}$) in TGA curves and exothermic peaks in DTA curves could be attributed to the decomposition of unreacted reactants present in the as prepared samples. Furthermore, in the third region (625 - 1000 $^\circ\text{C}$) the weight loss is due to the crystallization of the self combusted final product. It is noticed that, at third region the temperature required for crystallization is increased for the Gd^{3+} doped samples compared with pure CoFe_2O_4 . The higher the ionic radius of Gd^{3+} , more is the thermal energy required for crystallization and hence the resulting

crystallization occurs at relatively higher temperature for Gd^{3+} doped samples. It is concluded from the TG-DTA results that an optimal temperature of $750\text{ }^\circ\text{C}$ is suitable for annealing the as prepared samples and the samples are used for further characterization are annealed at $750\text{ }^\circ\text{C}$ for 2 h.

Powder x-ray diffraction study

The PXRD patterns of $\text{CoGd}_x\text{Fe}_{2-x}\text{O}_4$ powders are shown in Fig. 2. All the PXRD patterns confirm that the samples have a poly crystalline cubic spinel structure and the reflection planes are perfectly indexed to the cobalt ferrite (JCPDS NO: 03-0864). Furthermore, we have noticed that there is no evidence of secondary phase for $x \leq 0.10$. This confirms that the substituted Gd^{3+} ions are completely dissolved into the cobalt ferrite lattices. The emergence of small amount of orthoferrite phase GdFeO_3 (JCPDS No: 74-1900) also appear at higher Gd^{3+} content ($x > 0.10$). The ionic radius of Gd^{3+} ion is 0.938 \AA , which is higher than that of the Fe^{3+} ion (0.67 \AA), and hence the amount of Fe^{3+} ions replaced by Gd^{3+} ions are limited and there is a solubility limit for the replacement of Fe^{3+} ions by Gd^{3+} ions, thus it is expected that an excess substitution of Gd^{3+} ions tend to aggregate around the grain boundaries in the form of GdFeO_3 ³⁴. The optimized maximum dissolving limit for the Gd^{3+} ions into cobalt ferrite in the present work is $x = 0.10$. Since, the substitution of rare earth ions induces structural distortion by increasing crystal imperfection due to larger size and produces micro-strain, utilizing Williamson–Hall equation to analyze PXRD pattern is more appropriate than the Scherrer’s equation^{28, 35, 36}. The full width at half maximum (FWHM) of the experimental diffracted peaks is modeled to the Gaussian shape. The actual broadening (β) of diffraction pattern corrected for the experimental broadening (β_{ex}) and the instrumental broadening (β_{in}) as $\beta = \beta_{\text{ex}}^2 - \beta_{\text{in}}^2$. Considering the size and strain effect, the Williamson–Hall equation for actual broadening (β) can be modeled as follows,

$$\beta = (K\lambda/D \cos\theta) + 4\varepsilon \tan\theta \quad (1)$$

$(K\lambda/D \cos\theta)$ is broadening due to the size (D) and $4\varepsilon \tan\theta$ is broadening due to strain (ε). The modification of equation (1) yields,

$$\beta \cos\theta = (K\lambda/D) + 4\varepsilon \sin\theta \quad (2)$$

Where, β is the full width at half maximum of the PXRD peaks, θ is the position of the peaks, K is the Debye–Scherrer constant (0.94 for spherical shaped nanoparticles), λ is the x-ray wavelength, D is the size of the crystallite and ε is the average micro strain. Therefore, a linear plot of $\beta \cos\theta$ versus $4 \sin\theta$ yields intercept as crystallite size and the slope as strain. The Williamson-Hall plot for $\text{CoGd}_x\text{Fe}_{2-x}\text{O}_4$ nanoparticles are shown in Fig. 3. From the Fig. 3 it is noticed that the intercept values progressively increase to higher values and the slope of the plot changing from negative to the positive with Gd^{3+} content. The calculated values of the crystallite size are plotted and shown in Fig. 4. The size of the pure cobalt ferrite is 46 nm, which decreases for gadolinium doped cobalt ferrite as 24 nm ($\text{CoGd}_{0.05}\text{Fe}_{1.95}\text{O}_4$) and 23 nm ($\text{CoGd}_{0.10}\text{Fe}_{1.90}\text{O}_4$) respectively. It is noticed that the growth of the CoFe_2O_4 is restricted by the substitution of Gd^{3+} ions, leading to a relatively small crystallite size compared with pure cobalt ferrite. Due to the higher bond energy of $\text{Gd}^{3+}-\text{O}^{2-}$, as compared with that of $\text{Fe}^{3+}-\text{O}^{2-}$, it is obvious that more energy is required to incorporate Gd^{3+} ions into the octahedral site³⁷. The energy required for this process is supplied at the expense of crystallization and therefore hinder the growth of the crystallite and the smaller crystallite size is observed for Gd^{3+} doped samples. It is interesting to notice that for higher substitution ($x > 0.10$) of Gd^{3+} , the size of the crystallites slightly increases as 24 nm ($\text{CoGd}_{0.15}\text{Fe}_{1.85}\text{O}_4$) and 27 nm ($\text{CoGd}_{0.20}\text{Fe}_{1.80}\text{O}_4$) respectively. The sudden increase of the crystallite size for higher concentration ($x > 0.10$) of Gd^{3+} is expected due to the presence of

secondary GdFeO_3 phase. It is clear from the PXRD patterns of $\text{CoGd}_{0.15}\text{Fe}_{1.85}\text{O}_4$ and $\text{CoGd}_{0.20}\text{Fe}_{1.80}\text{O}_4$ that the higher concentration of Gd^{3+} favours the formation of the secondary GdFeO_3 phase. It is inferred from this observation that the part of the energy required for the incorporation of Gd^{3+} ions into octahedral sites during synthesis process is now being utilized for the growth of the crystallites. The values of average micro strain are measured from the slope of the lines using Fig. 3. The variation of slope value of the pure and Gd^{3+} doped cobalt ferrites obtained from Fig. 3 and plotted in Fig. 4. We have noticed that the slope of pure CoFe_2O_4 is negative. It is well known that for smallest particles the negative slope indicates the presence of compressive strain in the material, while the positive slope indicates the tensile strain³⁸. The negative slope of the CoFe_2O_4 indicates the presence of compressive strain. It is interesting to note that the doping of higher amount of Gd^{3+} ions shifting the slope values from negative to positive. This indicates that the substitution of larger size Gd^{3+} ions are expanding the crystal lattices by changing the strain from compressive to tensile. The variation of the lattice constant of all the samples calculated using the following relation³⁹.

$$a = (\lambda/2) * \sqrt{((h^2+k^2+l^2)/ \sin^2\theta)} \quad (3)$$

Where, a is the lattice constant, λ is the wavelength, $(h\ k\ l)$ is Miller indices and θ is the position of the peak. The variation of the lattice constant of pure and Gd^{3+} doped cobalt ferrite is given in Table 1. For pure cobalt ferrite, the calculated value of lattice constant is 8.371 Å, which is similar to that of the reported value for CoFe_2O_4 prepared using solid state reaction method³⁴. It is observed from the Table 1 that the Gd^{3+} substitution gradually increases the lattice constant up to $x = 0.15$ (8.382 Å). The ionic radius of the Gd^{3+} ion is higher than that of the Fe^{3+} ion; a linear expansion in the lattice constant is expected. The expansion of the lattice constant is further supporting the incorporation of Gd^{3+} into cobalt ferrite lattice. It is noticed that the value of

lattice constant is smaller for $\text{CoGd}_{0.20}\text{Fe}_{1.80}\text{O}_4$ (8.377 Å) compared with $\text{CoGd}_{0.15}\text{Fe}_{1.85}\text{O}_4$ (8.382 Å). It is clear from the PXRD patterns that the intensity of the secondary phase GdFeO_3 present in $\text{CoGd}_{0.20}\text{Fe}_{1.80}\text{O}_4$ is higher than that of the $\text{CoGd}_{0.15}\text{Fe}_{1.85}\text{O}_4$. The substituted higher amount of Gd^{3+} ions are not entering into the cobalt ferrite sub-lattices and forming more number of secondary GdFeO_3 phase and hence the reduced value of the lattice constant is observed. The values of x-ray density (d_x) have been estimated and presented in Table 1 using the relation $D_{hkl} = (8M/\text{Na}^3)^{39}$ where, D_{hkl} is the x-ray density, M is the molecular weight and N is the Avogadro number $6.023 \times 10^{23} \text{ mol}^{-1}$. The calculated value of the x-ray density is 5.314 g/cm^3 for CoFe_2O_4 . We have noticed that the x-ray density increases with Gd^{3+} substitution. The enhanced value of x-ray density is attributed to improved molecular weight of the samples having gadolinium ions. The density increases as the particles tend to acquire nano size and pack tightly.

Raman analysis

Raman spectroscopy is a powerful technique to provide more insights on the atomic structure of nanoparticles⁴⁰. The Raman spectra of $\text{CoGd}_x\text{Fe}_{2-x}\text{O}_4$ ($x = 0.0, 0.05, 0.10, 0.15$ and 0.20) samples are presented in Fig. 5. For a more accurate analysis the recorded Raman spectra have been deconvoluted into individual Lorentzian peaks and the positions of the bands are given in Table 2. Cobalt ferrite has cubic spinel structure with $Fd3m$ space group. From the group theory analysis, 39 normal modes of vibrations are predicted for spinel structure, out of which five modes A_{1g} (648–680 cm^{-1}), E_g (278–293 cm^{-1}), $3T_{2g}$ (539–565, 449–471 and 163–177 cm^{-1}) are Raman active^{41, 42}. It is noticed from the Table 2 that pure cobalt ferrite shows five major bands at ~ 197 , ~ 312 , ~ 471 , ~ 579 and $\sim 694 \text{ cm}^{-1}$ respectively. These bands are assigned to five Raman active modes of vibrations ($A_{1g} + E_g + 3T_{2g}$). Besides these bands, due to quantum-size effects a band around $\sim 621 \text{ cm}^{-1}$ is also detected⁴³. Furthermore, the recorded Raman spectra

confirms the spinel structure of cobalt ferrite and rules out the existence of impurities like α - Fe_2O_3 , which usually gives a strong bands at ~ 240 and $\sim 300 \text{ cm}^{-1}$. We have noticed that the incorporation of Gd^{3+} ion into the cobalt ferrite has slightly shifted the centre of the peaks towards the higher frequency side. The shifting of peaks are attributed to the development of micro strain in cobalt ferrite lattices due to the larger size Gd^{3+} ion substitution and further supporting the PXRD results. Moreover, it is interesting to note that the intensity of $A_{1g(2)}$ (621cm^{-1}) vibrational mode is gradually increased with the Gd^{3+} substitution. The use of Raman spectroscopy to reveal the degree of inversion of spinel ferrites has been highlighted by several authors^{42, 44-48}. Chandramohan *et al*⁴⁷. related the decrease in relative intensity ratio of $A_{1g(1)}$ and $A_{1g(2)}$ vibrational modes to the lowering of inversion parameter of cobalt ferrite nanoparticles of 6 nm size compared with 500 nm. Since, the T_{2g} modes are assigned to vibrations within octahedral sites, whereas the A_{1g} modes are related to vibrations within tetrahedral sites, Fernandes *et al*⁴². suggested that the contribution from the T_{2g} mode should also be considered for the analysis of the degree of inversion. It is further reported that for simple nanoferrites, the area ratio between the bands associated with the octahedral and tetrahedral sites, ie, $T_{2g(1)}/[A_{1g(1)} + A_{1g(2)}]$, is similar to the resultant degree of inversion. In our study, we have utilized both intensity ratio and area ratio methods and the obtained values of both ratio's are depicted in Fig. 6. It is noticed from the Fig. 6 that both ratio's are decreasing for Gd^{3+} doped cobalt ferrite nanoparticles and indicating the low degree of inversion of Gd^{3+} doped samples compared with the pure cobalt ferrite. It is well known that the vibrational modes above 600 cm^{-1} are corresponding to A_{1g} symmetry involving symmetrical stretching vibration of metal-oxygen bond at tetrahedral group (AO_4). The substitution of large size Gd^{3+} ions are expected to occupy only at the octahedral sites⁴⁹ by transferring Co^{2+} from octahedral sites to tetrahedral sites; hence

decreasing the degree of inversion which further confirms the variation in the cation distribution compared with pure cobalt ferrite.

Infrared spectral investigation

The FTIR spectra of pure and Gd^{3+} doped Co ferrite nanoparticles are also obtained and shown in Fig. 7. The position of vibrational bands of CoGd ferrites are given in Table 1. For spinel ferrites, the vibrational band around 600 cm^{-1} corresponds to the stretching vibration of tetrahedral groups and the vibrational band around 400 cm^{-1} corresponds to the stretching vibration of octahedral groups⁵⁰. It is noticed from the Table 1 that the vibrational spectra consist of two major absorption bands, first at about 600 cm^{-1} (ν_1) and second at about 400 cm^{-1} (ν_2). These absorption bands further confirm the formation of spinel structured cobalt ferrite. We have noticed that with the increase of the gadolinium ion doping, a small shift in the absorption bands of tetrahedral and octahedral sites are noticed towards the lower frequency side. The substitution of Gd^{3+} ions into the octahedral site migrate an equal number of Co^{2+} ions to the tetrahedral sites and, as a result, the equal number of Fe^{3+} ions are migrated from tetrahedral sites to octahedral sites to relax the strain²⁷. The ionic radius of Co^{2+} ion (0.82 \AA) is higher than that of Fe^{3+} ion (0.67 \AA), an increasing number of Co^{2+} ions in A sites is increasing ionic radii of the A sites. Similarly, an increasing number of Gd^{3+} ions in B sites increase the ionic radii of the B sites. The increase of ionic radii of A and B sites reduces the fundamental frequency and hence the central frequency of tetrahedral and octahedral sites shifted towards the lower frequency side. This further confirms the results discussed in Raman analysis.

FE-SEM and EDS analysis

To analyze surface morphological information, the FE-SEM images are observed for all the samples. Fig. 8 (a–e) shows the FE-SEM images of the pure and gadolinium doped cobalt ferrite samples. It is noticed from the images that pure cobalt ferrite particles are agglomerated spherical shaped and nano size. Moreover, the doping of Gd^{3+} ions decreases the size of the grains. A clear difference is observed between the un-doped and doped samples. This observation is in good agreement with the size reduction observed using PXRD analysis discussed earlier. The elemental analysis has been carried out for selected samples using energy dispersive spectroscopy with the help of FE-SEM and the results are shown in Fig. 9 (a-c). The obtained results confirm the presence of Co, Gd, Fe and O elements in the prepared samples and no other traceable impurities are found within the resolution limit of EDS.

Magnetic study

Magnetic hysteresis loop measurements of the pure and gadolinium doped cobalt ferrites nanoparticles are carried out at 300 K and 10 K. The hysteresis loops of $CoGd_xFe_{2-x}O_4$ ($x = 0.0, 0.05, 0.10, 0.15$ and 0.20) nanoparticles are shown in Fig. 10 (a, b). It is noticed that the pure and Gd^{3+} doped cobalt ferrite nanoparticles show ferrimagnetic behavior characterized by hysteresis loops with saturation magnetization, coercivity and remanance. The saturation magnetization (M_s), the coercivity (H_c) and the remanance magnetization (M_r) at 300 K and 10 K are given in Table 3. It is noticed that the values of saturation magnetization decrease for gadolinium doped cobalt ferrites. According to the Neel's sublattice model, the spinel ferrites have three types of interaction between tetrahedral (A) and octahedral (B) interstitial sites, such as A–A, B–B and A–B. Among these three interactions, A–B intra sublattice interaction is very stronger than the other two interactions⁵¹. It is well know that the substitution of rare earth ion

generally occupies the octahedral sites due to its larger ionic radius. The ordered magnetic moment of Gd^{3+} is evident at low temperature only (Curie temperature of Gd is $293.2^{\circ}K$ ⁵²). Therefore, the substitution of Gd^{3+} ions in cobalt ferrite lattices is equal to the substitution of non-magnetic atom at the B sites and hence reduces the magnetization of B sites. The total magnetization of cobalt ferrite is the difference between the magnetization of B and A sites, and subsequently reduces the magnetization at room temperature⁵³.

It is observed that for pure cobalt ferrite with the crystallite size of 46 nm, a M_s value of 80 emu/g is found at 300 K, which is in good agreement with the reported value (76 emu/g)⁵⁴. Moreover, the doping of Gd^{3+} ion in cobalt ferrite monotonically decreases the value of saturation magnetization from 80 to 53.8 emu/g when the crystallite size of Gd^{3+} doped cobalt ferrite decreases from 40 to 23 nm. Normally, it is attributed to the surface effect of the magnetic nanoparticles, due to small crystallite size¹². This surface effect can be elucidated by postulating the existence of dead magnetic layer due to the surface spin disorder. It is expected that the number of spins at the surface of Gd^{3+} doped cobalt ferrite increases as the crystallite size get smaller⁵⁵. It is further noticed from the PXRD analysis that for higher substitution of Gd^{3+} ions, small traces of secondary phase $GdFeO_3$ is noticed. The $GdFeO_3$ is antiferromagnetic in nature, a decrease in saturation magnetization expected for higher concentrations of gadolinium^{26, 56}. Thus, the resultant of the above mentioned effects are expected to reflect in the saturation magnetization of pure and gadolinium doped cobalt ferrite nanoparticles.

Moreover, it is observed that, at low temperature (10 K) the saturation magnetizations of all the samples are higher than that of 300 K. For pure cobalt ferrite, a M_s value of 86 emu/g is found at 10 K. Such increase in saturation magnetization compared with 300 K is attributed to the decrease of the thermal fluctuation and surface spin disorder at the surface of the nanoparticle.

We have noticed that there is no enhancement in the M_s value observed for Gd^{3+} substituted cobalt ferrite. Theoretically, it is expected to increase the magnetization of Gd^{3+} doped cobalt ferrite, due to the large magnetic moment of the Gd^{3+} ion (9.64 BM) at low temperature but, we have noticed that the value of saturation magnetization decreases with Gd^{3+} substitution. This could be attributed to the screening of Gd^{3+} magnetic contribution by the effect of smaller crystallites due to Gd^{3+} doping⁵⁷. This further indicates that the size effect plays an important role in magnetic properties of gadolinium doped cobalt ferrite nanoparticles.

The variation in the coercivity values (at 300 K and 10 K) with Gd^{3+} substitutions are given in Table 3. It is observed from Table 3 that the coercivity of $CoGd_xFe_{2-x}O_4$ nanoparticles at 300 K increases initially with x up to $x = 0.10$ and then decreases for higher ($x > 0.10$) Gd^{3+} substitution. Pure cobalt ferrite is having a coercivity of 1265 Oe, which increases to the 1635 Oe for $CoGd_{0.10}Fe_{1.90}O_4$. The observed variation in coercivity can be explained as follows. Similar to Co^{2+} ion, Gd^{3+} ion having stronger L-S coupling and weaker crystal field, which causes the stronger magnetocrystalline anisotropy of gadolinium doped cobalt ferrite⁵⁸. Furthermore, it is noticed that the crystallite size decreases for Gd^{3+} substituted samples. It is well known fact that coercivity is inversely proportional to the grain size⁵⁹. The bigger grains providing less pinning of domain walls due to the lower volume fraction of grain boundaries⁶⁰. The gradual enhancement of H_c with gadolinium content may be attributed to the decrease in grain size.

On the other hand, the presences of secondary phase also play an important role in influencing the coercivity of magnetic materials. We have observed that for the higher concentration of Gd^{3+} substitution ($x > 0.10$) the coercivity values are decreases. Generally, the secondary phases are distributed in grain boundaries of spinel ferrites and hinder the domain wall displacement; hence one can expect an enhancement in coercivity⁶¹. In our study, we have noticed that the variation in

coercivity does not follow the usual trend as above mentioned. It is well known that, in cobalt ferrite the magnetocrystalline anisotropy originates from the presence of Co^{2+} ions at the octahedral sites. As we have explained earlier in Raman analysis, the Co^{2+} ions are migrated from octahedral sites to tetrahedral sites due to large Gd^{3+} substitution. However, it is expected that the reduction in Co^{2+} ions in octahedral sites might be reducing the coercivity of gadolinium doped cobalt ferrite at higher concentrations. Furthermore, this clearly elucidate that the rearrangements of cation due to Gd^{3+} substitution plays a major role in variation of coercivity. At low temperature (10 K), the coercivity values of all the samples are one order of magnitude increased when compared with 300 K. It is seen that pure cobalt ferrite having a coercivity of 6747 Oe, which is increases to 13195 Oe for $\text{CoGd}_{0.10}\text{Fe}_{1.90}\text{O}_4$. The enhanced value of coercivity is attributed to the reduced thermal fluctuation energy at 10 K, which is less effective in reducing the effects of magnetocrystalline anisotropy energy. The substitution of rare earth ion is prone to cause magnetocrystalline anisotropy due to their larger size compared to transition elements and their lower value of magnetic moment, as well. The magnetocrystalline anisotropy constant (K_1) is determined by fitting high magnetic field data of hysteresis loop using the relation law of approach (LA) to saturation. Law of approach describes the dependence of magnetization (M) on applied magnetic field (H) for the applied magnetic field much higher than that of the coercive field (H_c). The dependence of magnetization near saturation can be written as follows⁶².

$$M = M_s \left[1 - \frac{b}{H^2} \right] + \kappa H \quad (4)$$

Where, M is the magnetization, M_s is saturation magnetization, $b = \frac{8}{105} \frac{K_1^2}{M_s^2 \mu_0^2}$, K_1 is the cubic anisotropy constant, μ_0 is the permeability of the free space, H is the applied magnetic field and κH is called as forced magnetization. The factor κH is applicable for high magnetic field and

high temperature data. In our case κH factor is not considered, since our data is at high field but not at high temperature. The calculated values of K_1 values are listed in Table 3 and the results shows that the value of K_1 strongly depends on both gadolinium content and temperature. Furthermore, our result is comparable to the earlier reports on cobalt ferrite nanoparticles^{63, 64}. It is noticed that at 300 K, the K_1 values increases with x up to $x=0.10$, thereafter it follows a decreasing trend. This reduction in K_1 value for higher concentration of Gd^{3+} is attributed to the non-incorporation of higher amount of Gd^{3+} ions in to cobalt ferrite lattices and the migration of Co^{2+} ions from octahedral sites to the tetrahedral sites.

Electrical properties

Dielectric constant

The dielectric response of all the samples are investigated to provide an insight into the electrical conduction mechanism of pure and gadolinium doped cobalt ferrite nanoparticles. The value of dielectric constant is obtained by using the formula $\varepsilon = C\varepsilon_0t/A$, where, C is the capacitance of the pellet, t is thickness of the pellet and A is the area of the pellet. The frequency dependence of the dielectric constant of pure and Gd^{3+} doped cobalt ferrites are measured at 30 °C in the frequency range of 100 Hz to 1 MHz and depicted in Fig. 11. It is seen from the Fig. 11 that the measured value of dielectric constant strongly depends on the frequency of applied electric field. It is further noticed from the Fig. 11 that the dielectric constant abruptly decreases at low frequencies and become constant at higher frequencies; hence showing a dispersion behavior at lower frequencies. The dispersion in dielectric constant is attributed to Maxwell-Wagner's type of interfacial polarization in agreement with Koop's phenomenological theory^{65, 66}. According to that the dielectric medium consists of well conducting grains and poorly conducting grain boundaries. It is well known that the polarization in ferrite is through a mechanism similar to the

conduction process⁶⁷. The polarization in cobalt ferrite is attributed to the electron hopping between $\text{Fe}^{2+} \leftrightarrow \text{Fe}^{3+}$ and hole hopping between $\text{Co}^{3+} \leftrightarrow \text{Co}^{2+}$ ions and hence charges carriers reaching the grain boundaries pile up there, due to the higher resistance and produce polarization. However, as the frequency of the applied electric field increases, the charge carriers can't follow the frequency of the alternating applied electric field and hence decrease the polarization⁶⁸. We have noticed that the dielectric constant of cobalt ferrite increases with the Gd^{3+} substitution. Similar kind of results also reported in literature for cobalt ferrite⁶⁹. This increase in dielectric constant could be attributed to the increasing number of Fe^{3+} ions at the octahedral site. As discussed earlier, the doping of Gd^{3+} ions migrate Co^{2+} ions to the tetrahedral sites to relax the strain, an equal amount of Fe^{3+} ions are migrating from tetrahedral site to octahedral sites and hence, increasing hopping of electrons between $\text{Fe}^{2+} \leftrightarrow \text{Fe}^{3+}$ ions in octahedral sites and enhances dielectric constant. It is noticed that for $\text{CoGd}_{0.20}\text{Fe}_{1.80}\text{O}_4$, the value of dielectric constant decreases compared with $\text{CoGd}_{0.15}\text{Fe}_{1.85}\text{O}_4$. Due to the non-incorporation of higher Gd^{3+} content in to CoFe_2O_4 , the transfer of Fe^{3+} ions from the tetrahedral sites to octahedral sites are limited. In addition to that, the formation of large number of GdFeO_3 secondary phase in $\text{CoGd}_{0.20}\text{Fe}_{1.80}\text{O}_4$, the number of Fe ions are decreases and ultimately $\text{Fe}^{2+} \leftrightarrow \text{Fe}^{3+}$ ion pairs. Hence, the availability of $\text{Fe}^{2+} \leftrightarrow \text{Fe}^{3+}$ ion pairs decreases at the octahedral sites, the hopping of electrons between $\text{Fe}^{2+} \leftrightarrow \text{Fe}^{3+}$ also decreases and reduces dielectric constant.

AC conductivity

As mentioned earlier, the mechanism of electrical conduction is the same as that of dielectric polarization in ferrites; the enhancement of electrical polarization could be better understood in terms of ac electrical conductivity analysis. The variation of frequency depended ac electrical conductivity of pure and gadolinium doped cobalt ferrite nanoparticles are depicted in Fig. 12. It

is obvious from the Fig. 12 that the electrical conductivity of all samples increases slowly at low frequencies and rapidly increases at higher frequencies. The frequency dependent variation of ac electrical conductivity has been explained on the basis of Maxwell–Wagner’s double layer model for dielectrics. At lower frequencies the resistive grain boundaries are more active; hence hopping of charge carriers between $\text{Fe}^{2+} \leftrightarrow \text{Fe}^{3+}$, $\text{Co}^{3+} \leftrightarrow \text{Co}^{2+}$ are very much hindered at lower frequencies and a constant plateau region is observed. However, at higher frequencies the conductive grains are more active and thereby supporting to the hopping of charge carriers between neighboring ions⁷⁰. Moreover, it is clear that the substitution of Gd^{3+} in cobalt ferrite enhances the conductivity and further supporting the mechanism for the enhancement in dielectric constant.

To get a clear insight into the conduction mechanism, ac electrical conductivity of all the samples measured for different temperature from 30 °C to 200 °C. Fig. 13 shows the reciprocal temperature dependence electrical conductivity (σ_{dc}) of $\text{CoGd}_x\text{Fe}_{2-x}\text{O}_4$ nanoparticles. We have noticed that the conductivity is found to increase with temperature as expected from the semiconducting behaviour of cobalt ferrite^{71, 72}. From the plot it is noticed that the conductivity reveals an Arrhenius-type temperature dependence given by the relation,

$$\sigma_{dc}(T) = \sigma_0 \exp(-E_{dc}/K_B T) \quad (5)$$

where, σ_0 is the pre-exponential factor, E_{dc} is the activation energy, K_B is the Boltzmann constant and T is the temperature in Kelvin. The activation energy, E_{dc} of all the samples are calculated from the slope of least square straight line fitting and the values of E_{dc} are given in Table 4. It is observed from the Table 4 that, the E_{dc} shows a dependence on the composition. It is well known that the electron hopping between $\text{Fe}^{2+} \leftrightarrow \text{Fe}^{3+}$ ions and the hole hopping between $\text{Co}^{3+} \leftrightarrow \text{Co}^{2+}$ ions in octahedral sites are responsible for electrical conduction and dielectric polarization in

cobalt ferrite. The decrease in activation energy with the increases in Gd^{3+} concentration supports the enhanced conductivity. Rahman *et al*³⁴. had been prepared Gd-substituted bulk cobalt ferrite using solid state reaction method and they found that the electrical conductivity decreases while the activation energy increases for Gd^{3+} doped samples. In this work, we found that the electrical conductivity increases and activation energy decreases. The decrease in activation energy is attributed to the redistribution of cations due to the small particle size. The calculated values of activation energy (0.408 - 0.347 eV) in the present study is comparable with those reported in literature and confirm the hopping of electrons are major responsible for electrical conduction³⁴. We have noticed that for $CoGd_{0.20}Fe_{1.80}O_4$, the electrical conductivity decreases compared with $CoGd_{0.15}Fe_{1.85}O_4$. Due to the non-incorporation of higher Gd^{3+} content in to $CoFe_2O_4$, the transfer of Fe^{3+} ions from the tetrahedral sites to octahedral sites are limited. In addition to that, the formation of large number of $GdFeO_3$ secondary phase in $CoGd_{0.20}Fe_{1.80}O_4$, the number of Fe ions are decreases and ultimately $Fe^{2+} \leftrightarrow Fe^{3+}$ ion pairs. Since, the hopping of electrons between $Fe^{2+} \leftrightarrow Fe^{3+}$ ions are responsible for electrical conduction, a decrease in $Fe^{2+} \leftrightarrow Fe^{3+}$ ion pairs decreases the hopping of electrons and also electrical conductivity of $CoGd_{0.20}Fe_{1.80}O_4$. Moreover, the higher value of activation energy of $CoGd_{0.20}Fe_{1.80}O_4$ (0.365 eV) compared with $CoGd_{0.15}Fe_{1.85}O_4$ (0.347 eV) supporting the above mechanism. It is concluded from the above discussions that, as crystallite size decreases the migration of Fe^{3+} from tetrahedral sites to octahedral sites play an important role in the conduction process of gadolinium doped cobalt ferrite nanoparticles.

Impedance analysis

Impedance spectroscopy is a powerful technique to analyse the electrical characteristics of heterogeneous materials⁷³. The dynamics of ac electrical conductivity is further understood from

the impedance spectra analysis of the pure and gadolinium doped cobalt ferrite nanoparticles in terms of grain and grain boundary. The measured complex impedance spectra ($-Z''$ vs Z') of pure and gadolinium doped cobalt ferrite samples are shown in Fig. 14 (a-e). The plot consists of a series array of two overlapping depressed semicircles, which represents the grain and grain boundary contribution to the conductivity. It is further noticed that, there is no other relaxation mechanism such as electrode effect has been noticed, which is usually present at the lower frequency side of the impedance spectra. The semicircle appears in the higher frequency region is the contribution from the grain conduction of the materials, which occurs due to parallel combination of the grain resistance and grain capacitance of the material. The semicircle appears in the lower frequency region is the contribution from the grain boundary conduction of the materials, which occurs due to parallel combination of the grain boundary resistance and grain boundary capacitance of the material. The observed semicircles in Fig. 14 successfully modelled by an equivalent circuit model (R_gCPE_g) ($R_{gb}CPE_{gb}$) where, R_g and R_{gb} are the resistance of grains and grain boundaries; CPE_g and CPE_{gb} are the constant phase element of grains and grain boundaries. A constant phase element (CPE) introduced in the circuit is due to the non-ideal behaviour of the capacitance⁷⁴. The values of R_g , R_{gb} , CPE_g and CPE_{gb} are obtained by fitting the impedance spectra for the proposed equivalent circuit model and the obtained results are presented in Table 4. It is noted that the values of R_{gb} , CPE_{gb} are higher than that of R_g , CPE_g . This indicates that the grain boundary contribution is higher than that of the grain contribution, which is due to the effect of small size crystallites. Furthermore, it is noticed that the value of $-Z''$ in the impedance plot for cobalt ferrite decrease with increasing gadolinium concentration and indicates that the overall resistance of the Gd^{3+} doped cobalt ferrite nanoparticles decreases.

Conclusion

The substitution of Gd^{3+} ions for Fe^{3+} in cobalt ferrite reduces the crystallite size and causes an appreciable change in the structural, magnetic and electrical properties to a large extent. The PXRD pattern revealed the formation of spinel $CoGd_xFe_{2-x}O_4$ ferrite with the signature of $GdFeO_3$ phases at higher concentration of gadolinium. Raman and FTIR spectroscopy analysis confirm the presence of tetrahedral and octahedral sites in prepared samples. The inversion degree of Gd^{3+} doped samples decreases compared with pure cobalt ferrite nanoparticles. It is found that with the increase of gadolinium concentration, the coercivity of cobalt ferrite nanoparticles is increased, the saturation magnetization decreased and magnetocrystalline anisotropy constant is increased due to crystallite size effect and cation distribution. The frequency dependent dielectric constant and the ac electrical conductivity increases with Gd-substitution. The behavior of dielectric constant and ac conductivity of pure and gadolinium doped cobalt ferrites found to follow Maxwell-Wagner's model. Further, the impedance plots show the decrease of resistance in terms of grain and grain boundary contributions. The obtained results demonstrate that the crystallite size, microstructure, magnetic and electrical properties can be tailored by tuning the gadolinium ion content in the cobalt ferrite. The enhanced coercivity (1635 Oe) with dielectric constant at room temperature of the prepared gadolinium doped cobalt ferrites is favorable for their potential use in high density recording media applications.

Acknowledgements

The authors thank the Central Instrumentation Facility, Pondicherry University for providing experimental facilities and UGC for financial support [F.No.39-489/2010]. The authors also thank centre for nanoscience and technology (C-NST), Pondicherry University for PXRD

measurements. CM thanks UGC for financial assistance in the form of Rajiv Gandhi National Fellowship (RGNF).

References

1. D. S. Mathew and R.S. Juang, *Chem. Eng. J.*, 2007, **129**, 51-65.
2. N. C. Pramanik, T. Fujii, M. Nakanishi and J. Takada, *J. Mater. Chem.*, 2004, **14**, 3328.
3. Z. H. Zhou, J. Wang, J. M. Xue and H. S. O. Chan, *J. Mater. Chem.*, 2001, **11**, 3110.
4. N. Rezlescu and E. Rezlescu, *Solid State Commun.*, 1993, **88**, 139.
5. P. S. A. Kumar, J. J. Shrotri, S. D. Kulkarni, C. E. Deshpande and S. K. Date, *Mater. Lett.*, 1996, **27**, 293.
6. A. C. F. M. Costa, E. Tortella, M. R. Morelli and R. H. G. A. Kiminami, *J. Magn. Magn. Mater.*, 2003, **256**, 174.
7. S. M. Chavan, M. K. Babrekar, S. S. More and K. M. Jadhav, *J. Alloys Compd.*, 2010, **507**, 21.
8. A. Broese van Groenou, P. F. Bongers and A. L. Stuyts, *Mater. Sci. Eng.*, 1969, **3**, 317.
9. G. Bate, *J. Magn. Magn. Mater.*, 1991, **100**, 413.
10. D. Carta, M. F. Casula, A. Falqui, D. Loche, G. Mountjoy, C. Sangregorio and A. Corrias, *J. Phys. Chem. C.*, 2009, **113**, 8606.
11. G. Hu, J. H. Choi, C. B. Eom, V. G. Harris and Y. Suzuki, *Phys. Rev B*, 2000, **62**, R779.
12. K. Maaz, A. Mumtaz, S. K. Hasanain and A. Ceylan, *J. Magn. Magn. Mater.*, 2007, **308**, 289.
13. C. Liu, B. Zou, A. J. Rondinone and Z. J. Zhang, *J. Am. Chem. Soc.*, 2000, **122**, 6263.
14. C. Murugesan, M. Perumal and G. Chandrasekaran, *Physica B*, 2014, **448**, 53.
15. R. K. Panda, R. Muduli and D. Behera, *J. Alloys Compd.*, 2015, **634**, 239.

16. R. M. Bozorth, E. F. Tilden and A. J. Williams, *Phys. Rev.*, 1955, **99**, 1788.
17. C. Sun, J. S. H. Lee and M. Zhang, *Adv. Drug Deliv. Rev.*, 2008, **60**, 1252.
18. G. Baldi, D. Bonacchi, M. C. Franchini, D. Gentili, G. Lorenzi, A. Ricci and C. Ravagli, *Langmuir*, 2007, **23**, 4026.
19. K. Stojak, S. Pal, H. Srikanth, C. Morales, J. Dewdney, T. Weller and J. Wang, *Nanotechnology*, 2011, **22**, 135602.
20. A. Hannour, D. Vincent, F. Kahlouche, A. Tchangoulian, S. Neveu and V. Dupuis, *J. Magn. Magn. Mater.*, 2014, **353**, 29.
21. L. M. Boutiuc, I. Dumitru, O. F. Caltun, M. Feder and V. Vilceanu, *Sens. Lett.*, 2009, **7**, 244.
22. B. I. Kharisov, H. V. R. Dias and O. V. Kharissova, *Arabian Journal of Chemistry*, DOI: <http://dx.doi.org/10.1016/j.arabjc.2014.10.049>.
23. J. K. Rajput and G. Kaur, *Chinese Journal of Catalysis*, 2013, **34**, 1697.
24. Q. Dai, D. Berman, K. Virwani, J. Frommer, P.O. Jubert, M. Lam, T. Topuria, W. Imaino and A. Nelson, *Nano Lett.*, 2010, **10**, 3216.
25. L. Zhao, H. Yang, X. Zhao, L. Yu, Y. Cui and S. Feng, *Mater. Lett.*, 2006, **60**, 1.
26. J. Jing, L. Liangchao and X. Feng, *Journal of Rare Earths*, 2007, **25**, 79.
27. R. C. Kambale, K. M. Song, Y. S. Koo and N. Hur, *J. Appl. Phys.*, 2011, **110**, 053910.
28. A. A. Kadam, S. S. Shinde, S. P. Yadav, P. S. Patil and K. Y. Rajpure, *J. Magn. Magn. Mater.*, 2013, **329**, 59.
29. K. K. Bharathi, G. Markandeyulu and C. Ramana, *J. Phys. Chem. C.*, 2010, **115**, 554.
30. F. Cheng, C. Liao, J. Kuang, Z. Xu, C. Yan, L. Chen, H. Zhao and Z. Liu, *J. Appl. Phys.*, 1999, **85**, 2782.

31. M. A. Ahmed, N. Okasha and S. I. El-Dek, *Nanotechnology*, 2008, **19**, 065603.
32. A. A. Sattar, *J. Mater. Sci.*, 2004, **39**, 451.
33. A. Sutka and G. Mezinskis, *Frontiers of Materials Science*, 2012, **6**, 128.
34. M. T. Rahman and C. V. Ramana, *J. Appl. Phys.*, 2014, **116**, 164108.
35. A. Khorsand Zak, W. H. Abd. Majid, M. E. Abrishami and R. Yousefi, *Solid State Sciences*, 2011, **13**, 251.
36. V. D. Mote, Y. Purushotham and B. N. Dole, *Journal of Theoretical and Applied Physics*, 2012, **6**, 1.
37. J. A. Dean, *Lange's handbook of chemistry*, McGraw-Hill, New York, 15th edn, 1998.
38. A. Ahlawat, V. G. Sathe, V. R. Reddy and A. Gupta, *J. Magn. Magn. Mater.*, 2011, **323**, 2049.
39. B. D. Cullity and S. R. Stock, *Elements of X-Ray Diffraction*, Prentice-Hall, New York, 3rd edn., 2001.
40. C. S. S. R. Kumar, *Raman Spectroscopy for Nanomaterials Characterization*, Springer, Heildeberg, Germany, 2012.
41. P. R. Graves, C. Johnston and J. J. Campaniello, *Mater. Res. Bull.*, 1988, **23**, 1651.
42. C. Fernandes, C. Pereira, M. P. Fernandez-Garcia, A. M. Pereira, A. Guedes, R. Fernandez-Pacheco, A. Ibarra, M. R. Ibarra, J. P. Araujo and C. Freire, *J. Mater. Chem. C.*, 2014, **2**, 5818.
43. C. Pereira, A. M. Pereira, C. Fernandes, M. Rocha, R. Mendes, M. P. Fernández-García, A. Guedes, P. B. Tavares, J.-M. Grenèche, J. P. Araújo and C. Freire, *Chem. Mater.*, 2012, **24**, 1496.

44. M. N. Iliev, P. Silwal, B. Loukya, R. Datta, D. H. Kim, N. D. Todorov, N. Pachauri and A. Gupta, *J. Appl. Phys.*, 2013, **114**, 033514.
45. R. Pazik, E. Piasecka, M. Malecka, V. G. Kessler, B. Idzikowski, Z. Sniadecki and R. J. Wiglusz, *RSC Advances*, 2013, 3, 12230.
46. M. N. Iliev, D. Mazumdar, J. X. Ma, A. Gupta, F. Rigato and J. Fontcuberta, *Phys. Rev B.*, 2011, **83**, 014108.
47. P. Chandramohan, M. P. Srinivasan, S. Velmurugan and S. V. Narasimhan, *J. Solid State Chem.*, 2011, **184**, 89.
48. M. A. Laguna-Bercero, M. L. Sanjuán and R. I. Merino, *J. Phys.: Condens. Matter*, 2007, **19**, 186217.
49. G. Kumar, J. Shah, R. K. Kotnala, P. Dhiman, R. Rani, V. P. Singh, G. Garg, S. E. Shirsath, K. M. Badoo and M. Singh, *Ceram. Int.*, 2014, **40**, 14509.
50. R. D. Waldron, *Phys. Rev.*, 1955, **99**, 1727.
51. K. J. Standley, *Oxide magnetic materials*, Oxford University Press, 1972.
52. H. E. Nigh, S. Legvold and F. H. Spedding, *Phys. Rev.*, 1963, **132**, 1092.
53. P. Kumar, S. K. Sharma, M. Knobel, J. Chand and M. Singh, *J. Electroceram.*, 2011, **27**, 51.
54. S. Singhal, T. Namgyal, S. Bansal and K. Chandra, *Journal of Electromagnetic Analysis and Applications*, 2010, **2**, 6.
55. R. H. Kodama, A. E. Berkowitz, J. E. J. McNiff and S. Foner, *Phys. Rev. Lett.*, 1996, **77**, 394.
56. M. A. Gilleo, *J. Chem. Phys.*, 1956, **24**, 1239.
57. S. R. Naik and A. V. Salker, *J. Mater. Chem.*, 2012, **22**, 2740.

58. S. Amiri and H. Shokrollahi, *J. Magn. Magn. Mater.*, 2013, **345**, 18.
59. M. Ishaque, M. Azhar Khan, I. Ali, H. M. Khan, M. Asif Iqbal, M. U. Islam and M. F. Warsi, *J. Magn. Magn. Mater.*, 2014, **372**, 68.
60. M. A. Khan, M. Javid ur Rehman, K. Mahmood, I. Ali, M. Niaz Akhtar, G. Murtaza, I. Shakir and M. Farooq Warsi, *Ceram. Int.*, 2015, **41**, 2286.
61. A. M. Pachpinde, M. M. Langade, K. S. Lohar, S. M. Patange and S. E. Shirsath, *Chem. Phys.*, 2014, **429**, 20.
62. S. Chikazumi, *Physics of Ferromagnetism*, Oxford University Press, Oxford, 1997.
63. A. Franco Jr and V. Zapf, *J. Magn. Magn. Mater.*, 2008, **320**, 709.
64. L. Kumar and M. Kar, *J. Magn. Magn. Mater.*, 2011, **323**, 2042.
65. J. C. Maxwell, *Electricity and Magnetism*, Oxford Univ. Press, London, 1973.
66. C. G. Koops, *Phys. Rev.*, 1951, **83**, 121.
67. K. Iwachi, *Jpn. J. Appl. Phys.*, 1971, **10**, 1520.
68. N. Sivakumar, A. Narayanasamy, C. N. Chinnasamy and B. Jeyadevan, *J. Phys.: Condens. Matter*, 2007, **19**, 386201.
69. A. Rana, O. P. Thakur and V. Kumar, *Mater. Lett.*, 2011, **65**, 3191.
70. K. Verma, A. Kumar and D. Varshney, *J. Alloys Compd.*, 2012, **526**, 91.
71. I. H. Gul and A. Maqsood, *J. Alloys Compd.*, 2008, **465**, 227.
72. I. H. Gul, A. Maqsood, M. Naeem and M. N. Ashiq, *J. Alloys Compd.*, 2010, **507**, 201.
73. J. R. Macdonald and E. Barsoukov, *History*, 2005, **1**, 8.
74. M. Younas, M. Nadeem, M. Atif and R. Grossinger, *J. Appl. Phys.*, 2011, **109**, 093704.

Figures

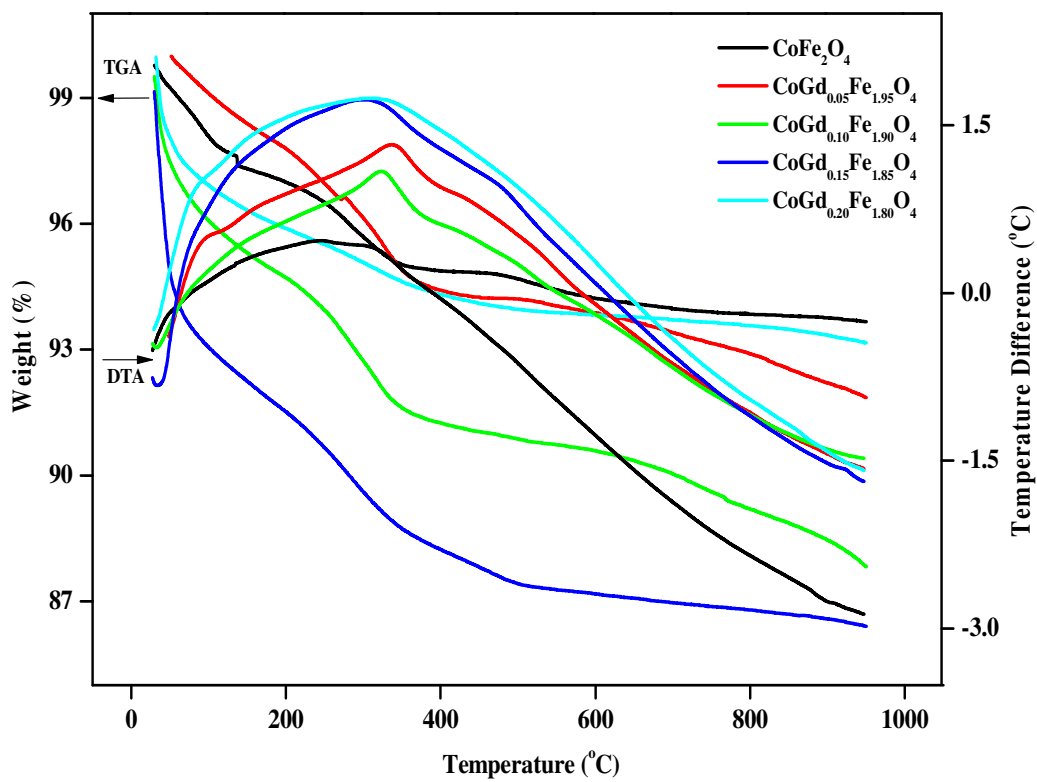


Fig. 1. TG-DTA curves of the pristine $\text{CoGd}_x\text{Fe}_{2-x}\text{O}_4$ powder samples.

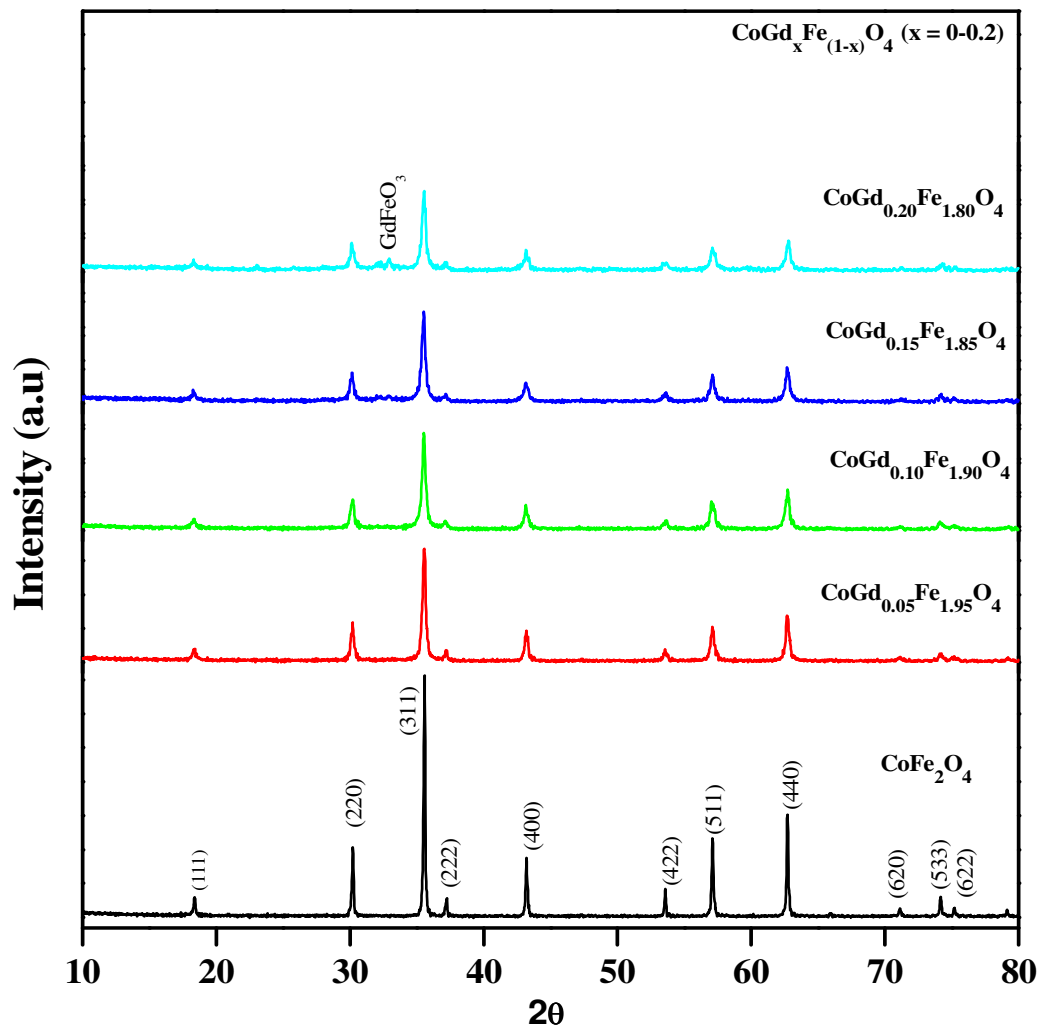


Fig. 2. Powder-XRD patterns of CoGd_xFe_{2-x}O₄ nanoparticles.

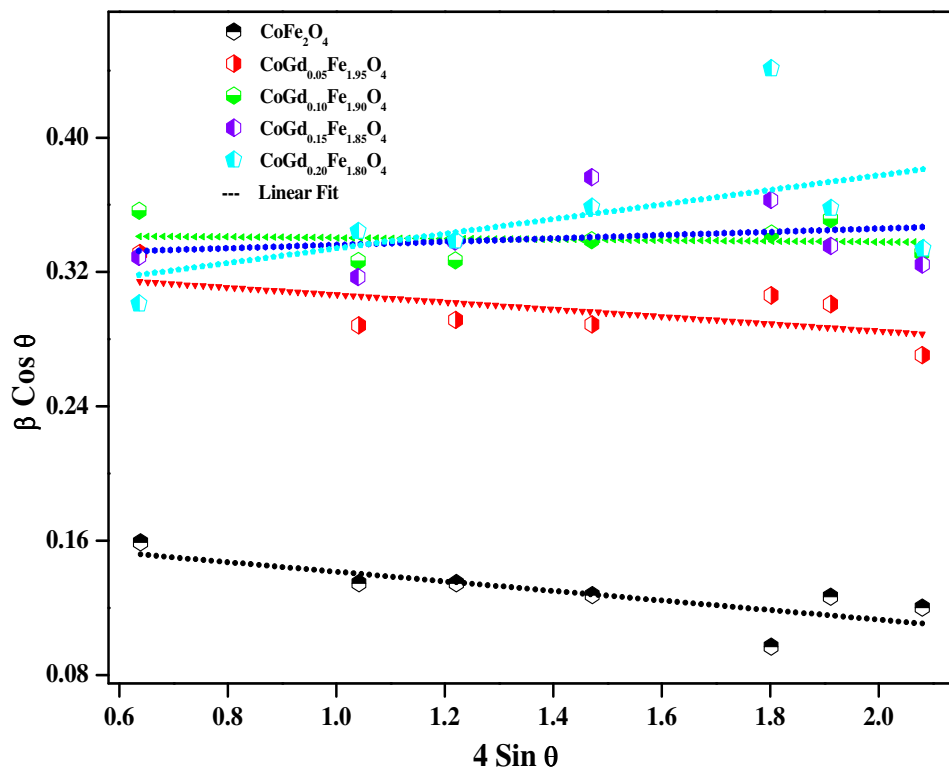


Fig. 3. Williamson-Hall plots of $\text{CoGd}_x\text{Fe}_{2-x}\text{O}_4$ nanoparticles

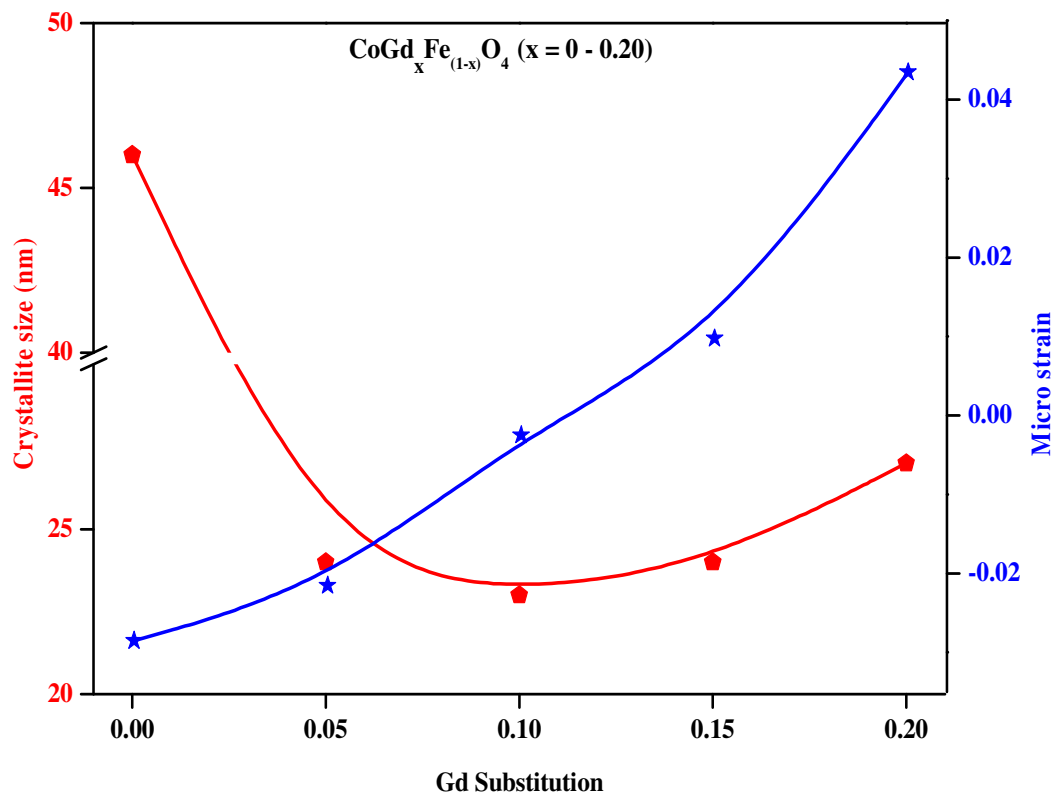


Fig. 4. Variation of the crystallite size and micro strain of $\text{CoGd}_x\text{Fe}_{2-x}\text{O}_4$ nanoparticles.

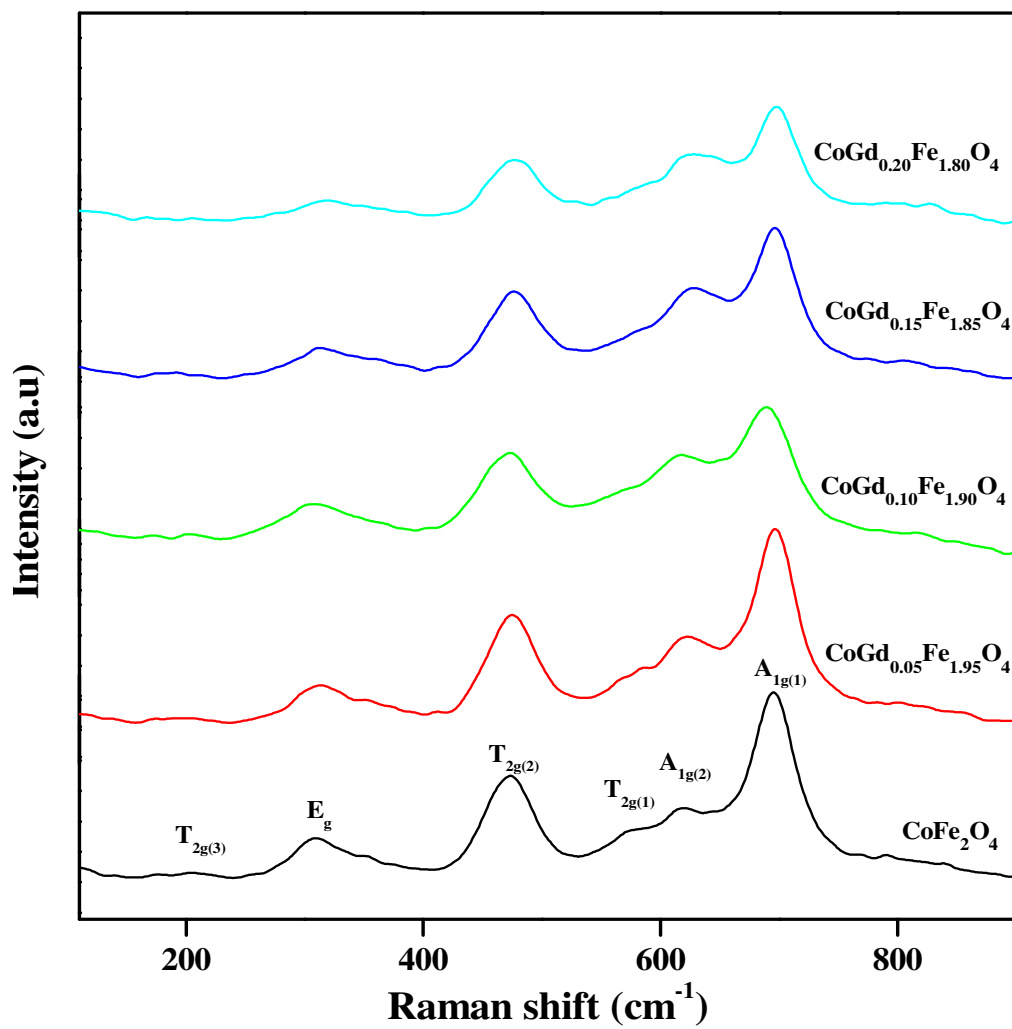


Fig. 5. Raman spectra of $\text{CoGd}_x\text{Fe}_{2-x}\text{O}_4$ nanoparticles.

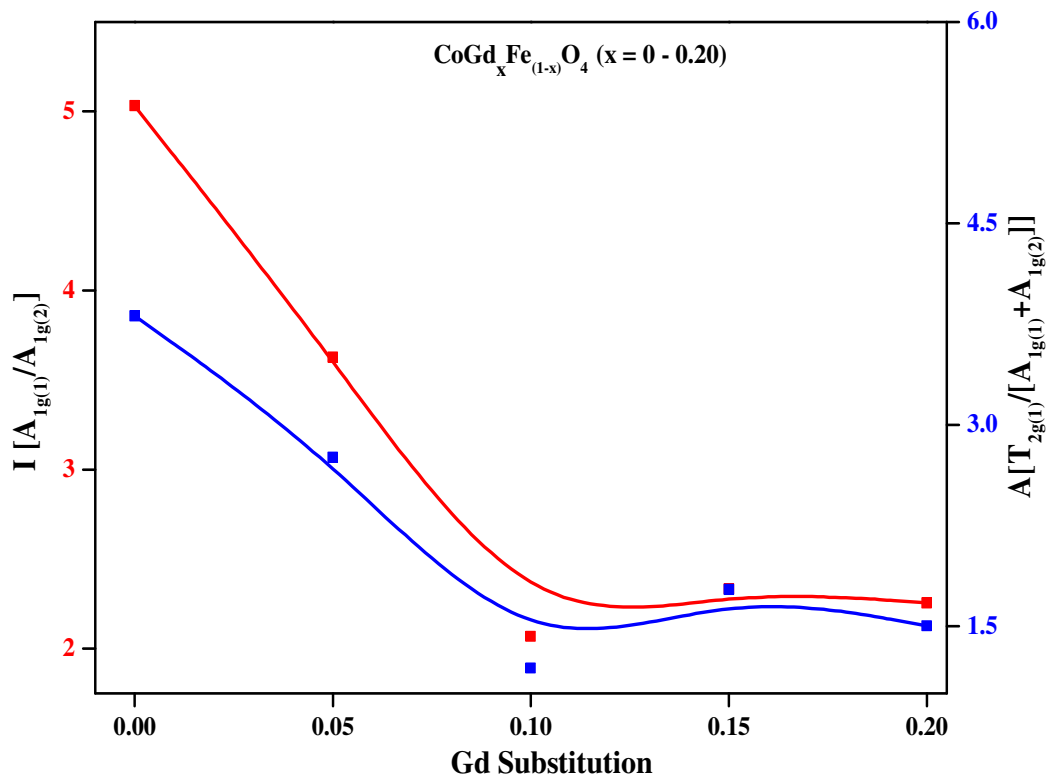


Fig. 6. Intensity and area ratio's of the Raman bands as a function of gadolinium content.

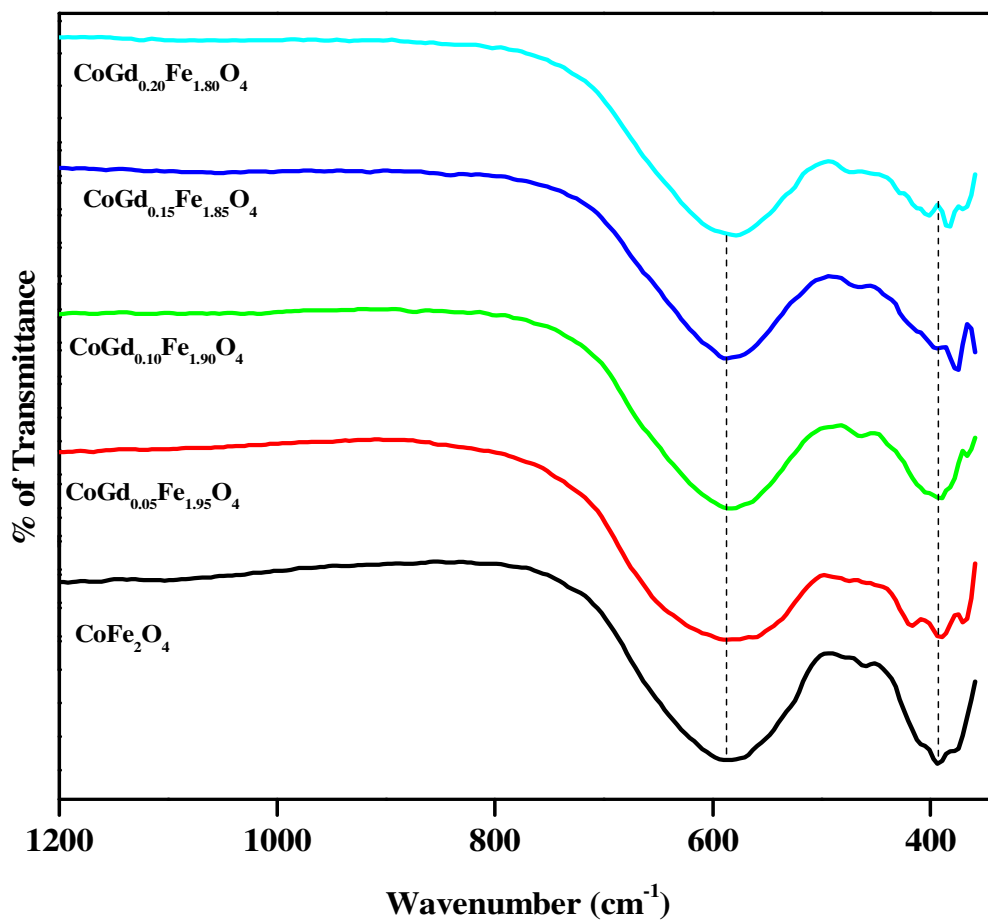
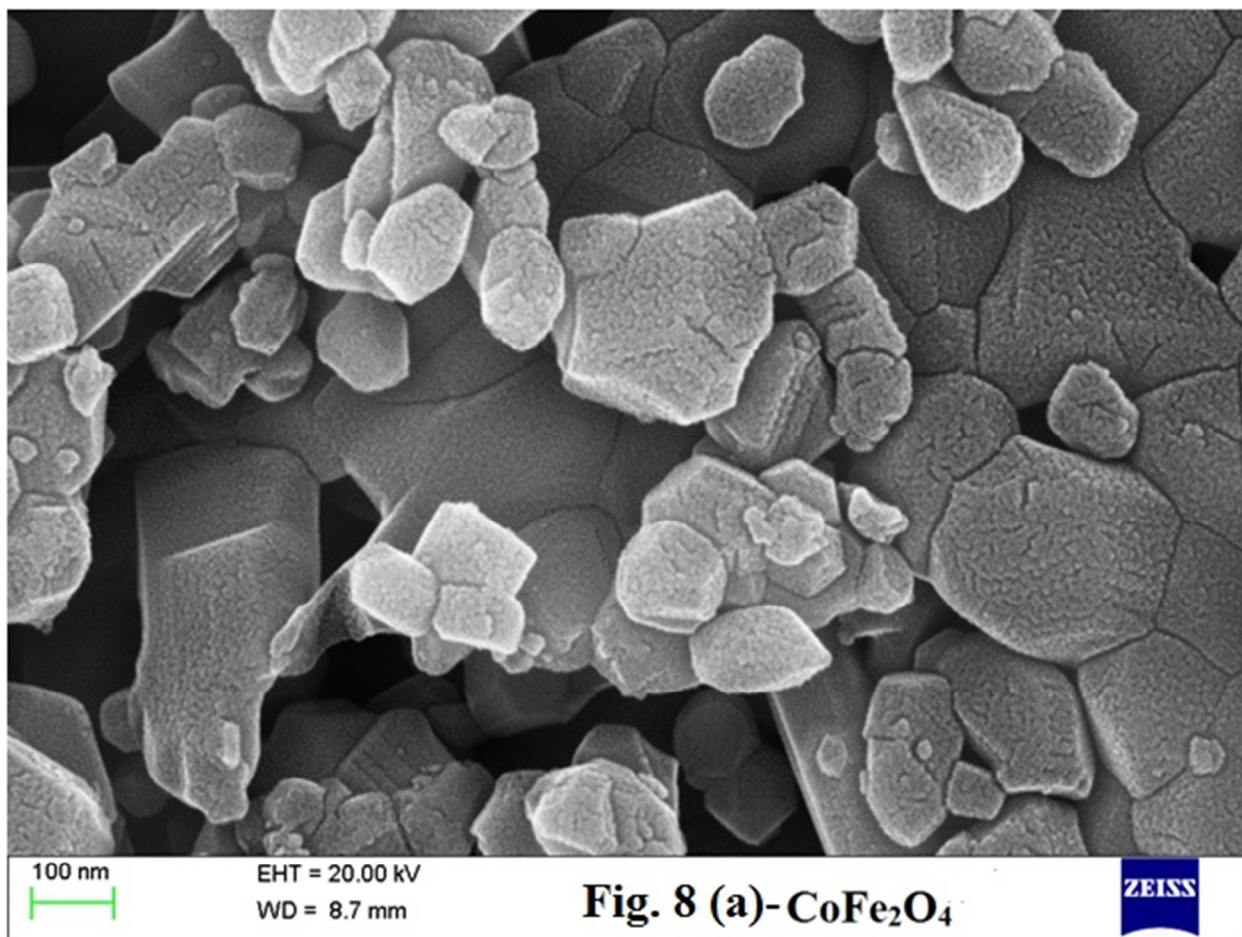
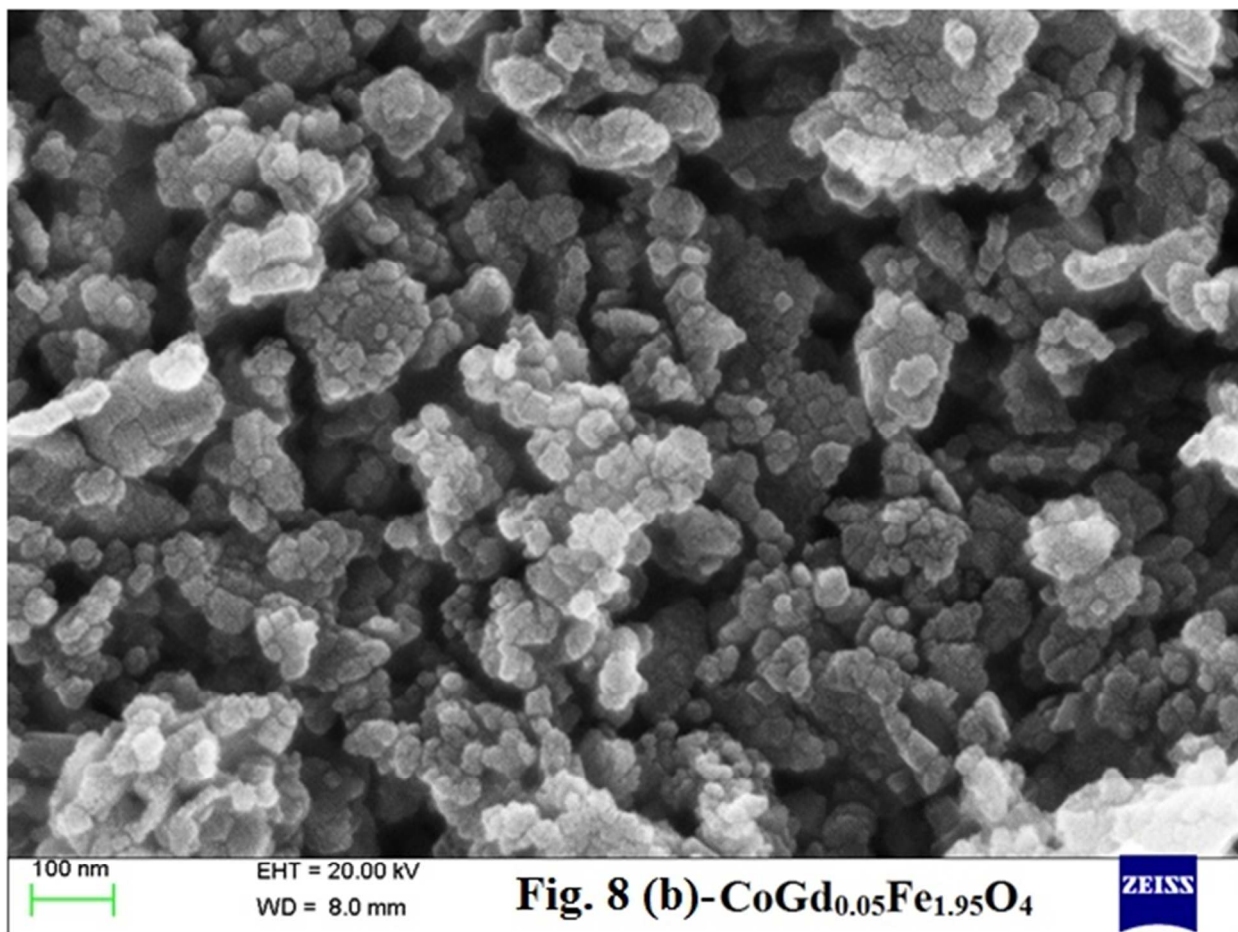
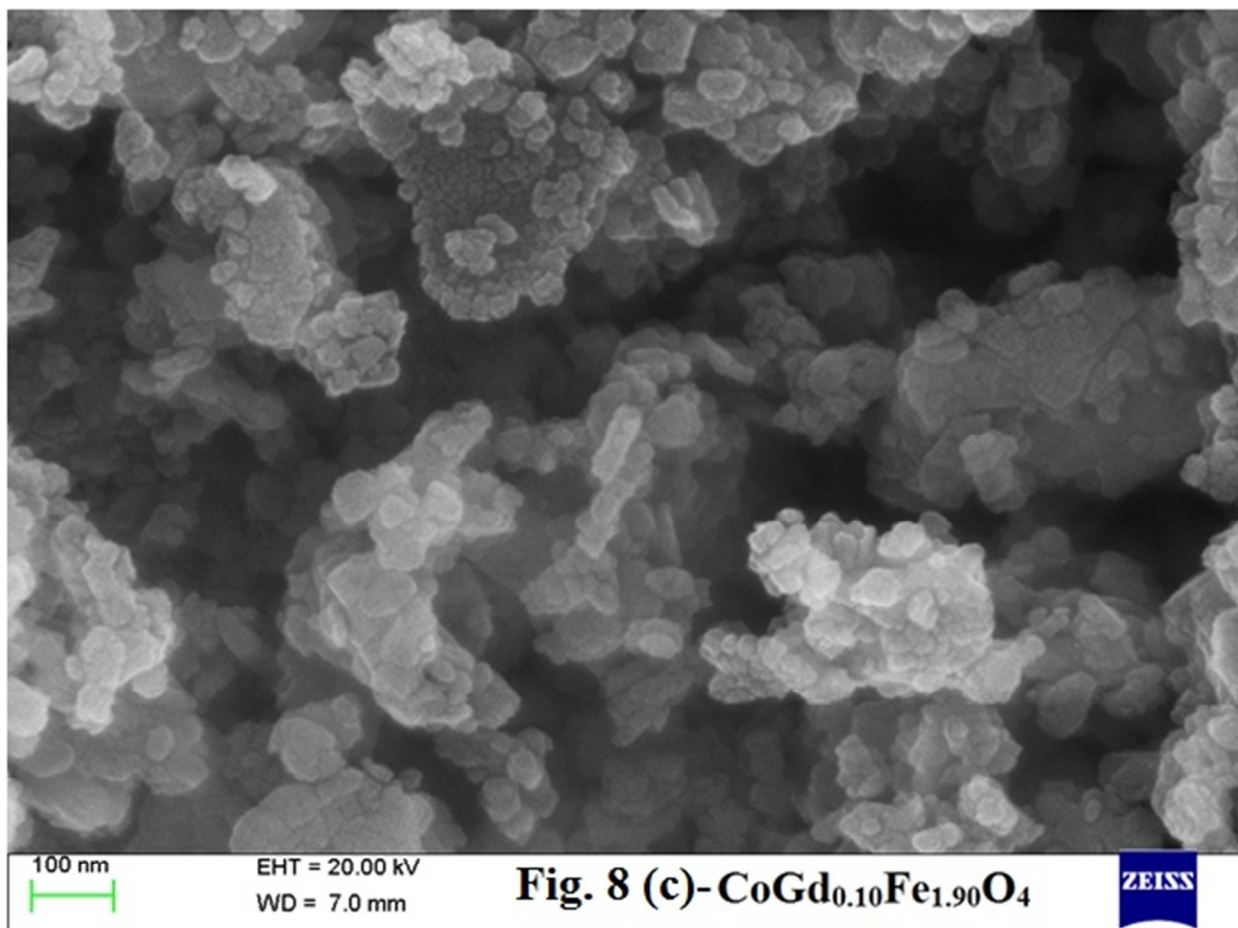
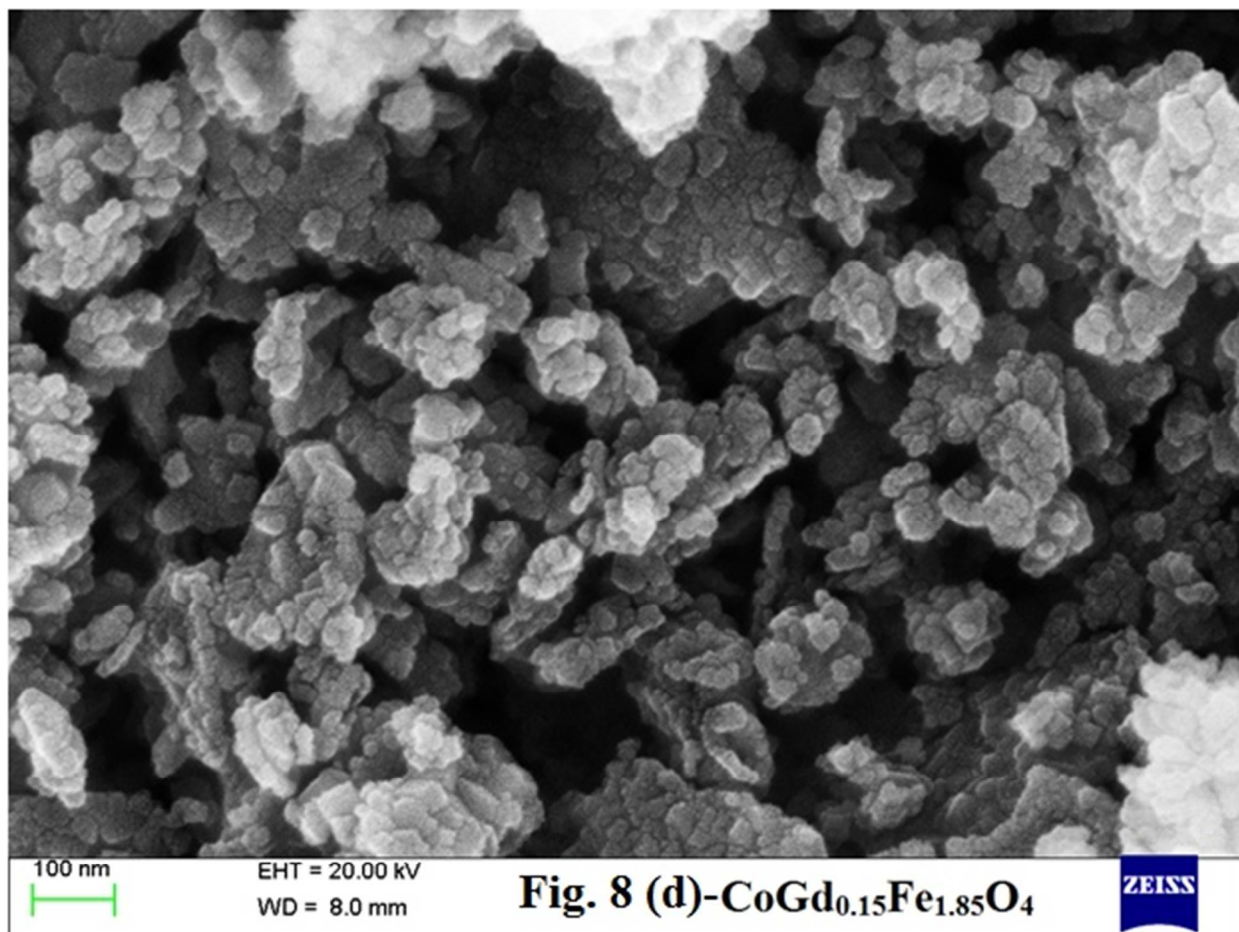


Fig. 7. The FTIR spectra of $\text{CoGd}_x\text{Fe}_{2-x}\text{O}_4$ nanoparticles.









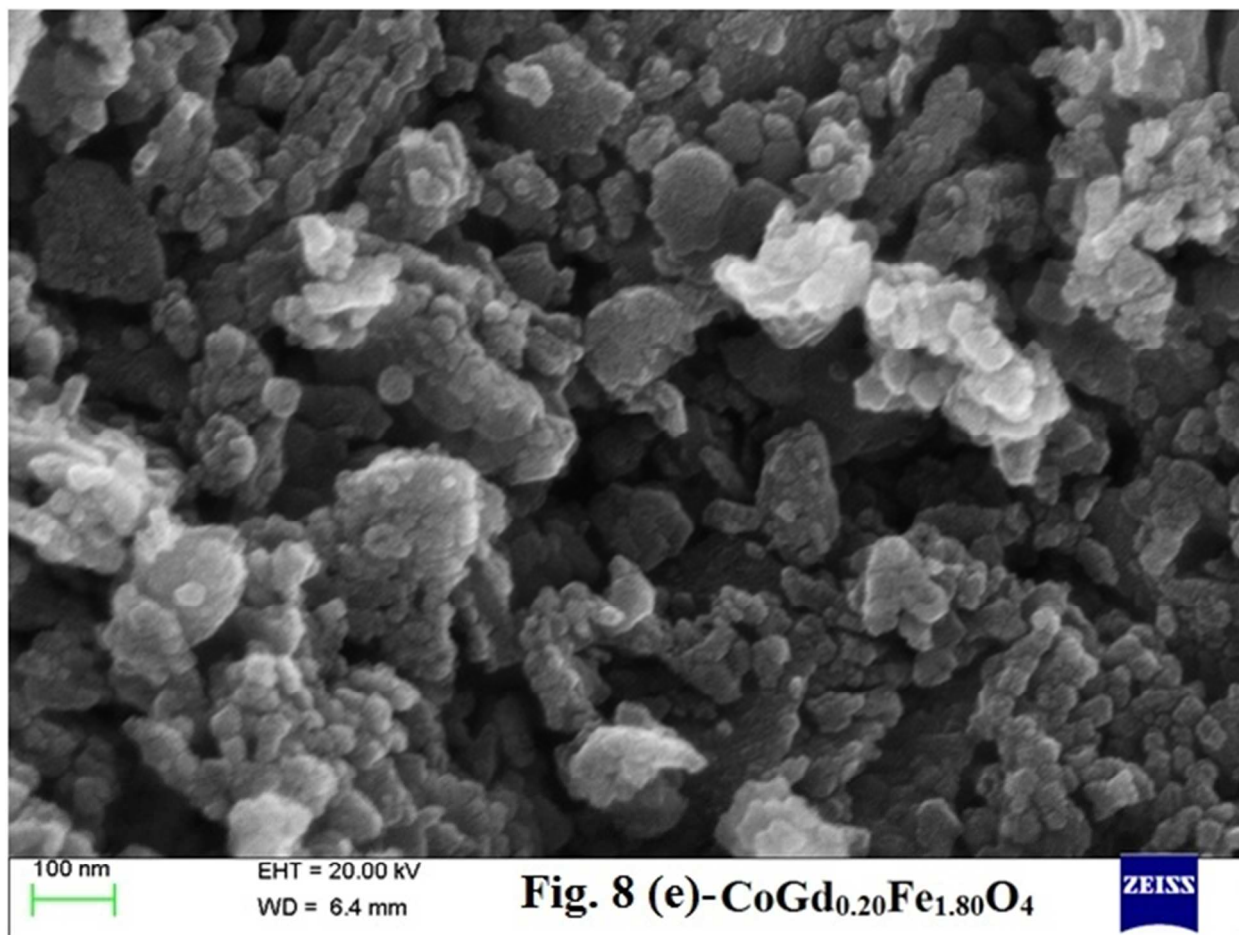


Fig. 8 (a-e). FE-SEM images of $\text{CoGd}_x\text{Fe}_{2-x}\text{O}_4$ nanoparticles.

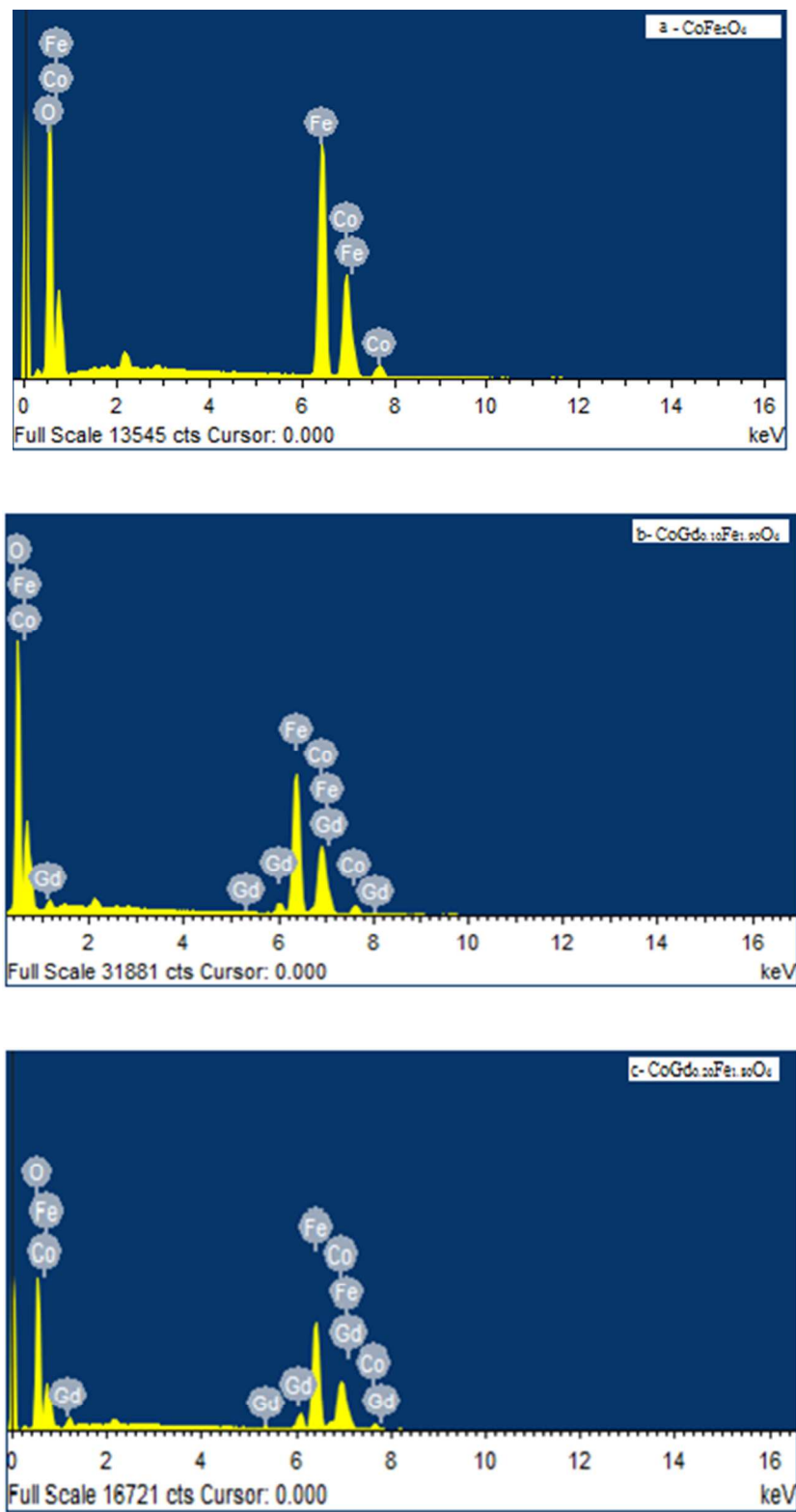


Fig. 9 (a-c). EDS spectra of $\text{CoGd}_x\text{Fe}_{2-x}\text{O}_4$ ($x = 0.0, 0.10$ and 0.20) nanoparticles.

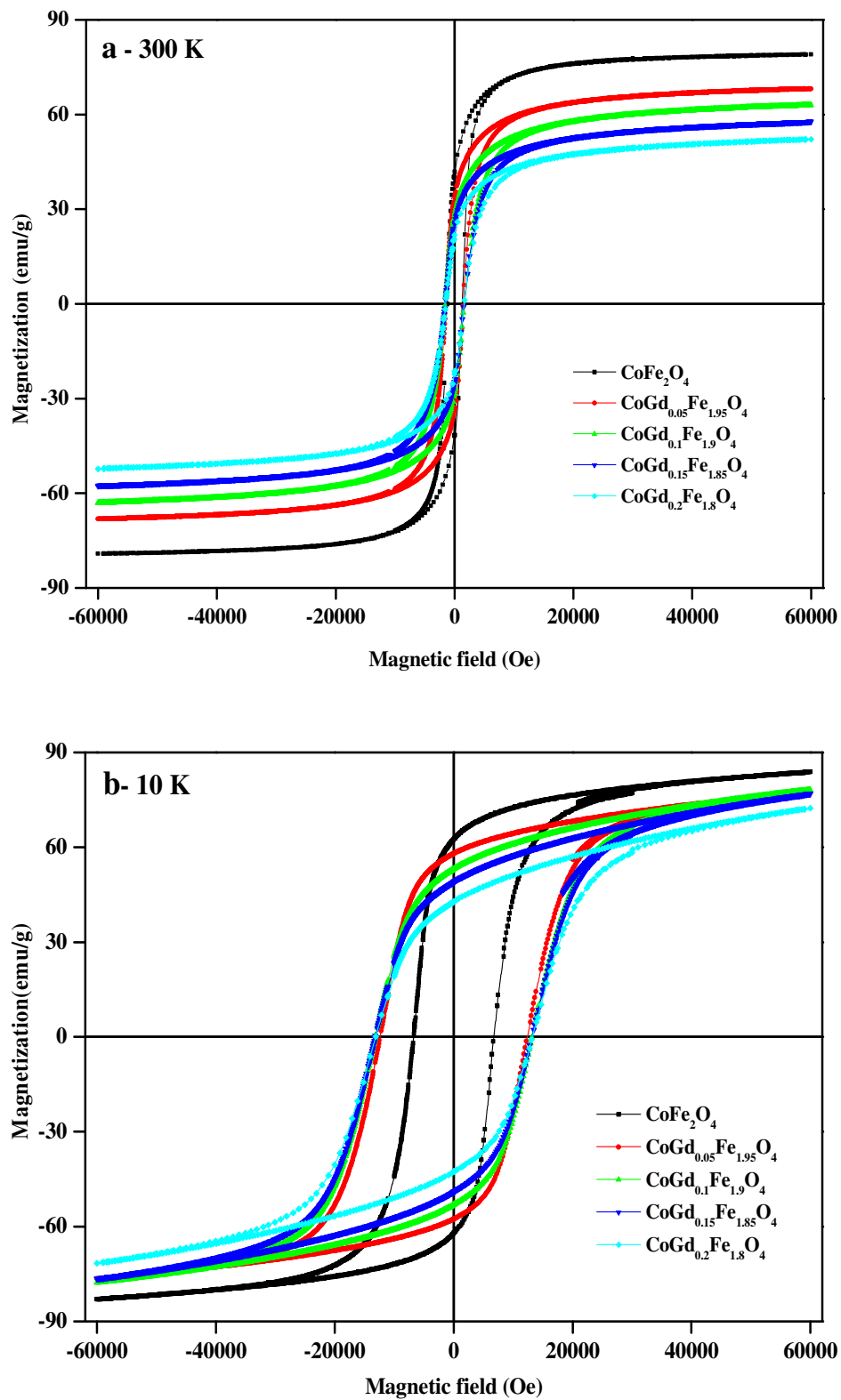


Fig. 10 (a, b). Hysteresis curves of $\text{CoGd}_x\text{Fe}_{2-x}\text{O}_4$ nanoparticles at (a) 300 K and (b) 10 K.

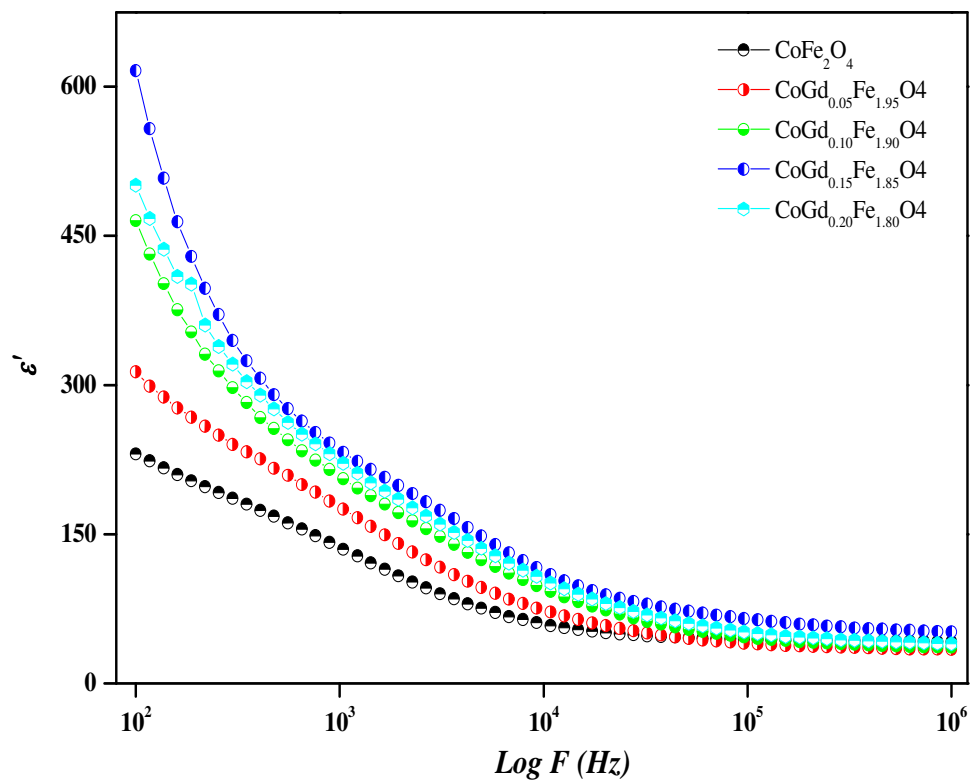


Fig. 11. The variation of dielectric constant with frequency of CoGd_xFe_{2-x}O₄ nanoparticles at 30 °C.

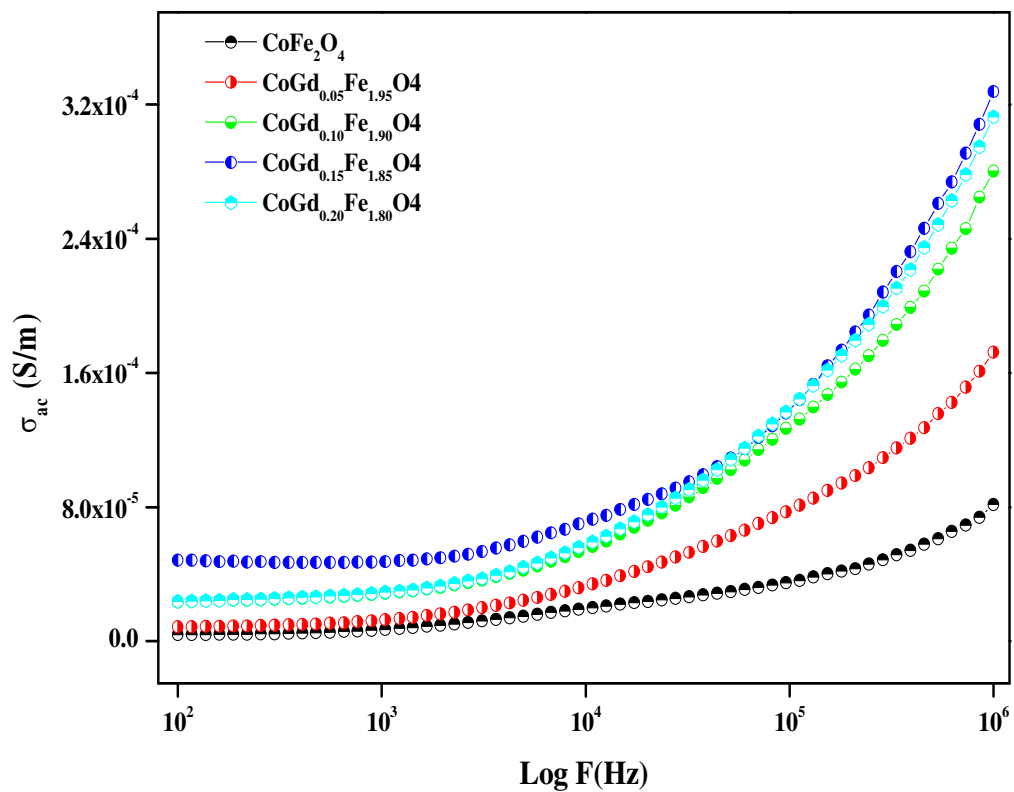


Fig. 12. The variation of frequency dependent ac electrical conductivity of $\text{CoGd}_x\text{Fe}_{2-x}\text{O}_4$ nanoparticles at 30 °C.

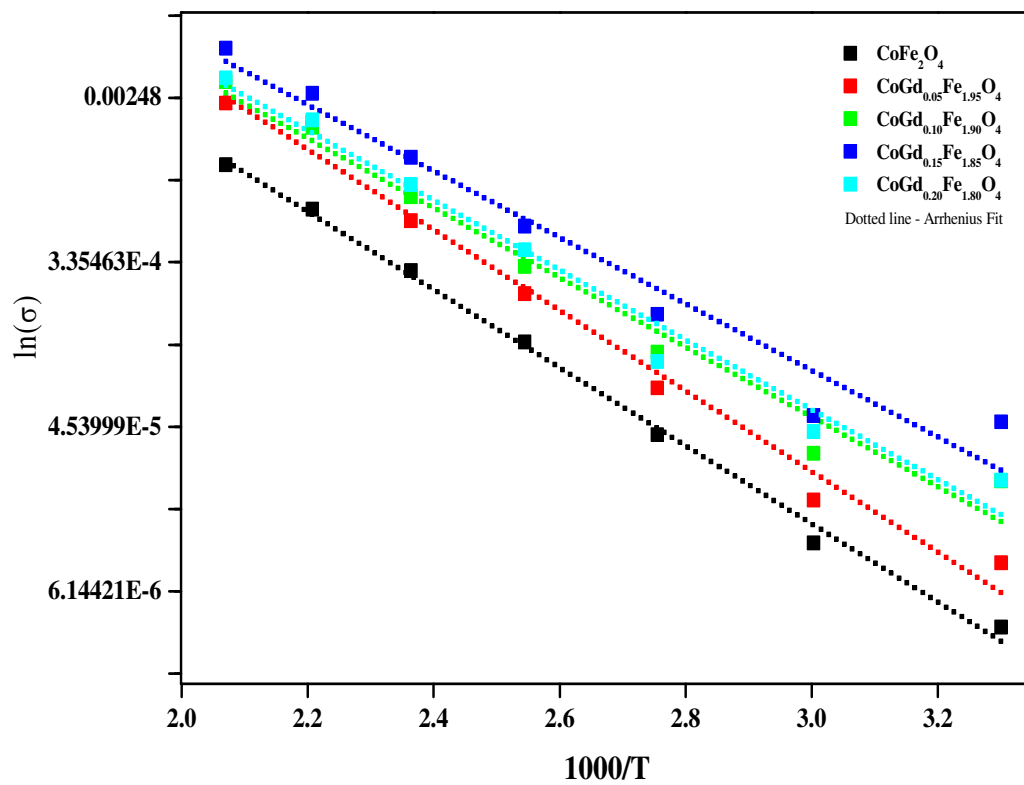
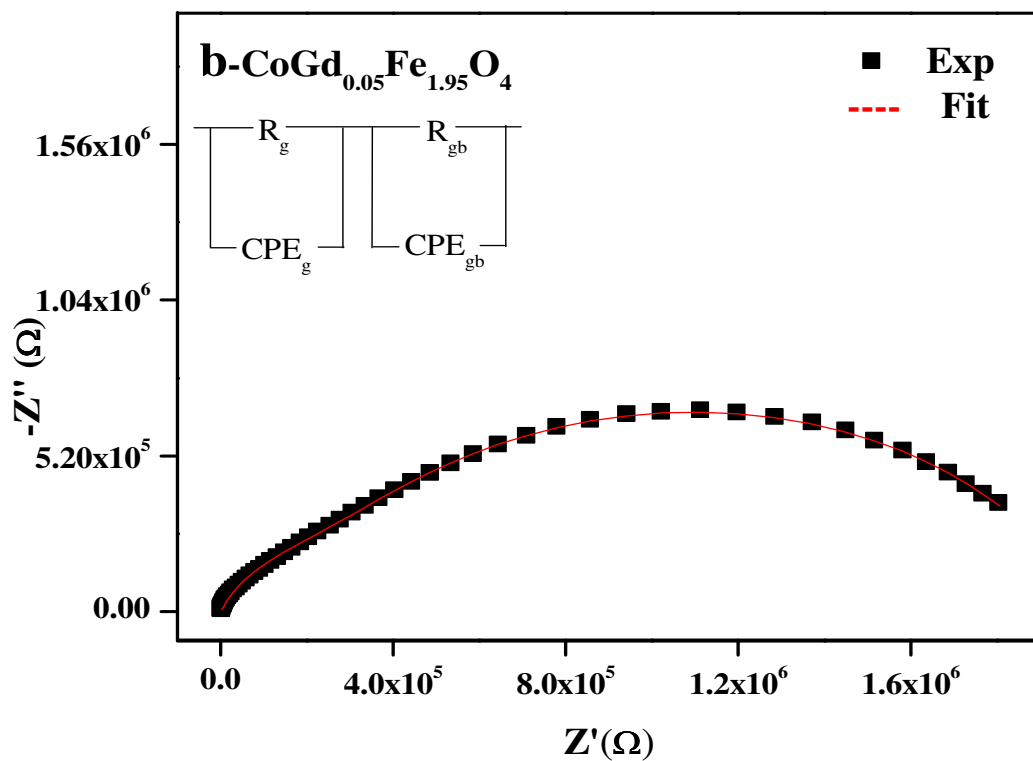
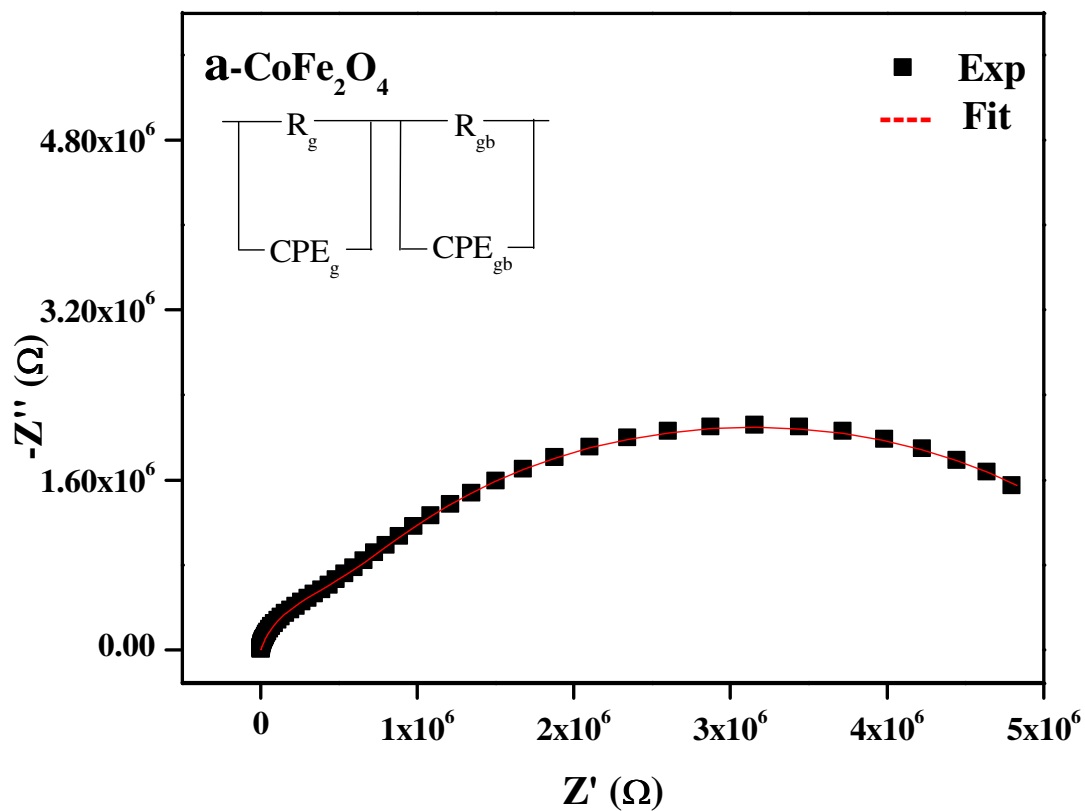
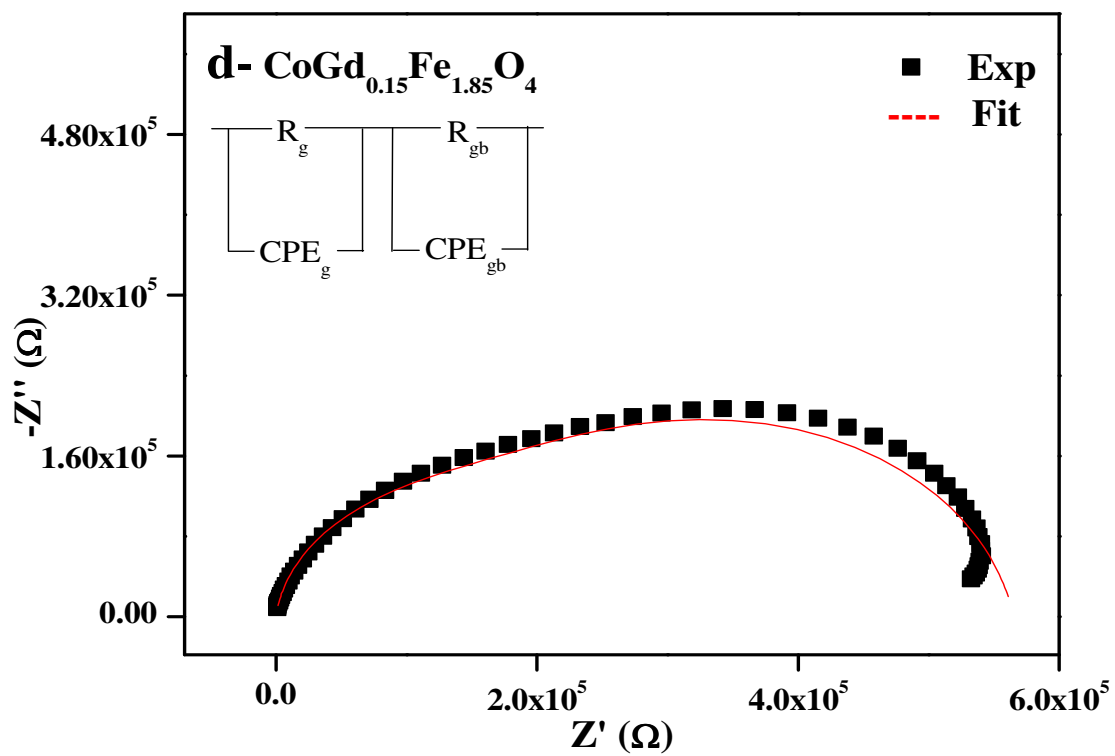
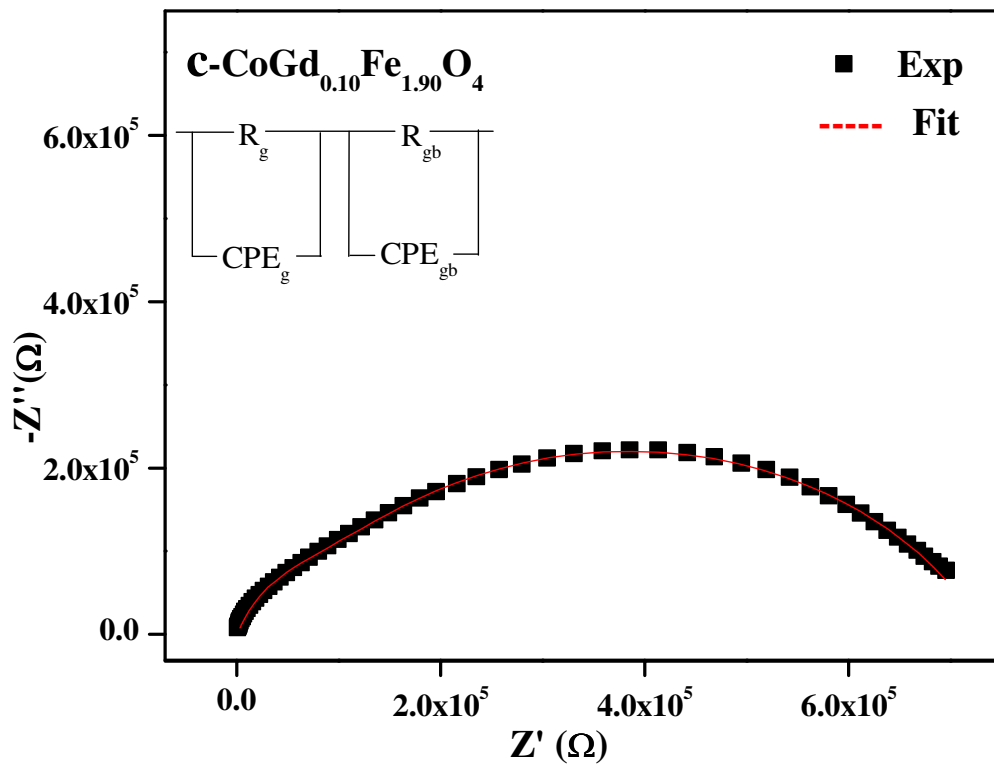


Fig. 13. Arrhenius plots for the dc conductivity for CoGd_xFe_{2-x}O₄ nanoparticles.





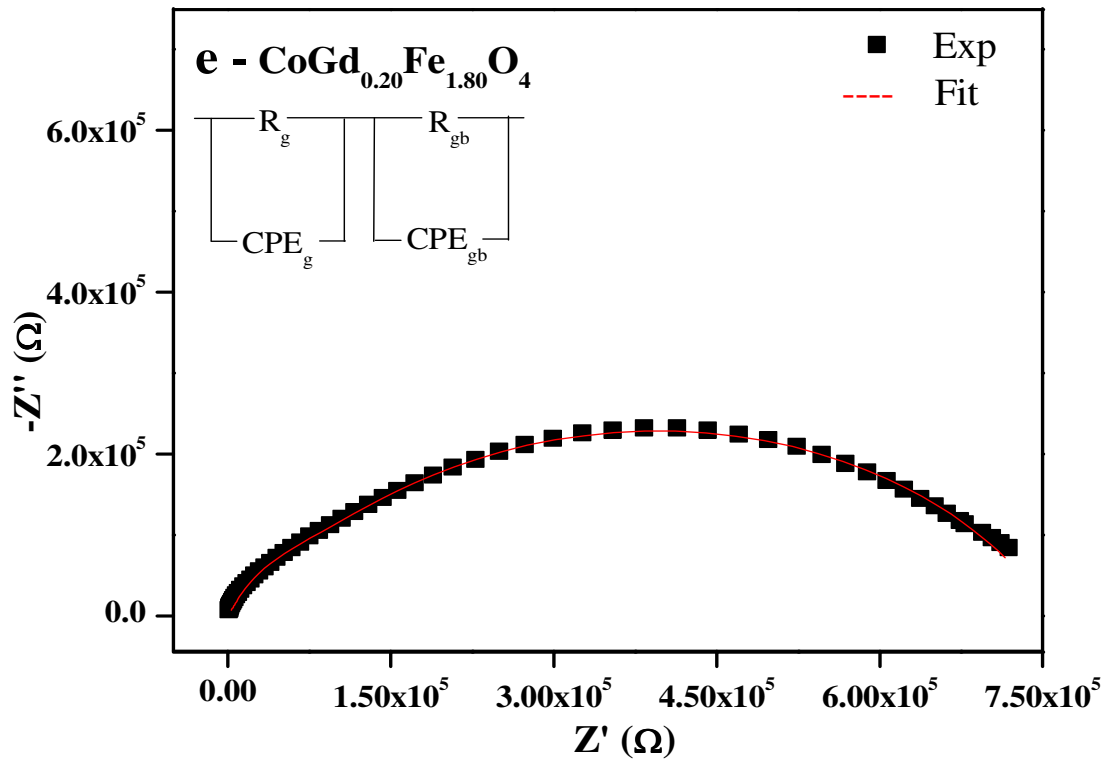


Fig. 14 (a-e). The impedance plot of $\text{CoGd}_x\text{Fe}_{2-x}\text{O}_4$ nanoparticles at $30\text{ }^\circ\text{C}$.

Table 1. Microstructural parameters: Lattice constant (a), x-ray density (d_x) and IR vibrational bands from XRD and FTIR analysis of $\text{CoGd}_x\text{Fe}_{2-x}\text{O}_4$ nanoparticles.

Sample	a (Å)	d_x (g/cm ³)	FTIR bands	
			ν_1 (cm ⁻¹)	ν_2 (cm ⁻¹)
CoFe_2O_4	8.370	5.313	586.31	393.45
$\text{CoGd}_{0.05}\text{Fe}_{1.95}\text{O}_4$	8.375	5.420	586.31	389.59
$\text{CoGd}_{0.10}\text{Fe}_{1.90}\text{O}_4$	8.379	5.527	582.46	389.59
$\text{CoGd}_{0.15}\text{Fe}_{1.85}\text{O}_4$	8.382	5.635	586.31	374.16
$\text{CoGd}_{0.20}\text{Fe}_{1.80}\text{O}_4$	8.377	5.759	578.60	381.87

Table 2. Raman peaks of $\text{CoGd}_x\text{Fe}_{2-x}\text{O}_4$ nanoparticles.

Sample	A_{1g} (1)	A_{1g} (2)	T_{2g} (1)	T_{2g} (2)	E_g (1)	T_{2g} (3)
CoFe_2O_4	694.83	621.21	579.20	471.49	312.31	197.3
$\text{CoGd}_{0.05}\text{Fe}_{1.95}\text{O}_4$	696.08	623.89	583.57	473.89	314.74	194.00
$\text{CoGd}_{0.10}\text{Fe}_{1.90}\text{O}_4$	689.06	621.98	575.05	471.50	308.54	201.61
$\text{CoGd}_{0.15}\text{Fe}_{1.85}\text{O}_4$	696.15	630.13	584.83	474.69	320.30	185.61
$\text{CoGd}_{0.20}\text{Fe}_{1.80}\text{O}_4$	697.39	630.72	589.14	475.43	322.70	171.04

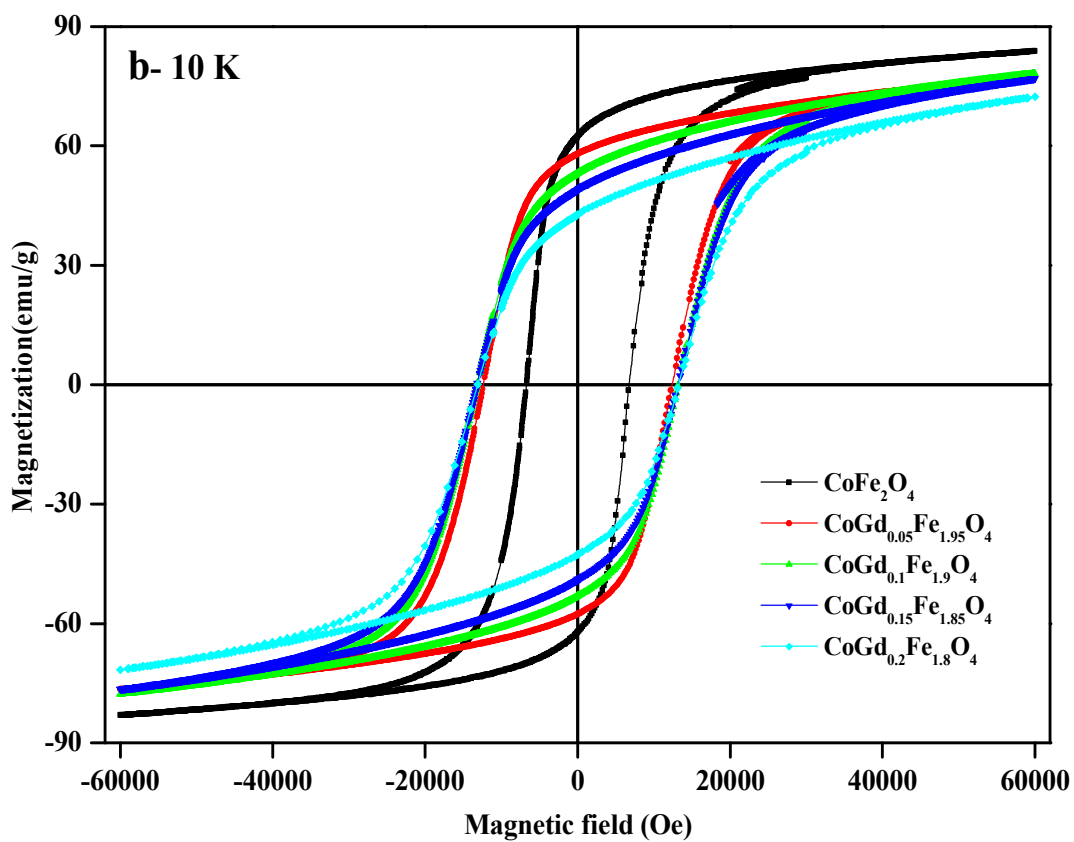
Table 3. Magnetic properties of $\text{CoGd}_x\text{Fe}_{2-x}\text{O}_4$ nanoparticles at 300 and 10 K: saturation magnetization (M_s), coercivity (H_c) remanent magnetization (M_r), and anisotropy constant (K_1).

Sample	300 K				10 K			
	M_s	H_c	M_r	$K_1 \times 10^6$	M_s	H_c	M_r	$K_1 \times 10^6$
	(emu/g)	(Oe)	(emu/g)	(erg/cm ³)	(emu/g)	(Oe)	(emu/g)	(erg/cm ³)
CoFe_2O_4	80.00	1265	41.60	0.583	86.12	6747	62.27	3.575
$\text{CoGd}_{0.05}\text{Fe}_{1.95}\text{O}_4$	69.47	1466	33.55	2.080	80.71	12400	57.77	4.008
$\text{CoGd}_{0.10}\text{Fe}_{1.90}\text{O}_4$	64.66	1635	27.91	2.231	83.25	13195	53.07	4.694
$\text{CoGd}_{0.15}\text{Fe}_{1.85}\text{O}_4$	59.24	1566	25.04	2.129	82.94	13184	48.98	5.039
$\text{CoGd}_{0.20}\text{Fe}_{1.80}\text{O}_4$	53.80	1560	21.62	2.009	78.51	13172	42.66	5.081

Table 4. Electrical properties: dielectric constant (ϵ'), ac conductivity(σ_{ac}), activation energy(E_{dc}), grain resistance(R_g), grain boundary resistance(R_{gb}), grain capacitance(CPE_g), grain boundary capacitance(CPE_{gp}).

Sample	ϵ'	σ_{ac}	E_{dc}	R_g	R_{gb}	CPE_g	CPE_{gp}
	at 100 Hz	(S/m) at 100 Hz					
CoFe_2O_4	230	3.97	0.408	4.55	5.44	9.77	3.52
$\text{CoGd}_{0.05}\text{Fe}_{1.95}\text{O}_4$	313	8.66	0.393	2.44	1.76	0.44	7.78
$\text{CoGd}_{0.10}\text{Fe}_{1.90}\text{O}_4$	465	2.34	0.365	4.48	0.69	8.54	1.67
$\text{CoGd}_{0.15}\text{Fe}_{1.85}\text{O}_4$	616	4.83	0.347	1.64	0.40	9.21	3.35
$\text{CoGd}_{0.20}\text{Fe}_{1.80}\text{O}_4$	501	2.37	0.365	0.376	0.72	0.10	0.173

Graphical Abstract



Hysteresis curves of $\text{CoGd}_x\text{Fe}_{2-x}\text{O}_4$ nanoparticles at 10 K.